Chemical Science

ROYAL SOCIETY OF CHEMISTRY

REVIEW

View Article Online
View Journal

Cite this: DOI: 10.1039/d6sc00001k

Photoluminescence of ligand-protected gold nanoclusters: progress in experimental and theoretical studies

Kang Li,[a] Pu Wang *[a] and Yong Pei *[ab]

Ligand-protected gold nanoclusters, with their small sizes and atomically precise structures, exhibit unique photophysical properties that position them as promising candidates for applications in bioimaging, sensing, and optoelectronics. However, except for a few ligand-protected gold nanoclusters, their photoluminescence quantum yield (PLQY) is still relatively low, and the underlying emission mechanisms are not yet fully elucidated. This review highlights recent experimental and theoretical advances aimed at enhancing and elucidating the photoluminescence (PL) mechanisms of ligand-protected gold nanoclusters. Experimentally, strategies such as heterometallic doping, ligand engineering, and structural rigidification have been employed to promote radiative transitions and suppress nonradiative decay, resulting in substantial improvements in PLQY. Theoretically, methods including density functional theory (DFT), time-dependent density functional theory (TDDFT), and nonadiabatic molecular dynamics (NA-MD) have provided important insights into the PL origin, emission pathways, and excited-state dynamics of ligand-protected gold nanoclusters. These advances will deepen our understanding of structure–property relationships in ligand-protected gold nanoclusters and pave the way for the rational design of highly emissive gold nanoclusters.

Received 1st January 2026
Accepted 26th February 2026

DOI: 10.1039/d6sc00001k

rsc.li/chemical-science

1. Introduction

Owing to their ultrasmall size (1–3 nm) and atomically precise structures, ligand-protected gold nanoclusters exhibit unique physical and chemical properties that distinguish them from traditional gold nanoparticles (>3 nm, characterized primarily by surface plasmon resonance). In particular, they display rich photoluminescence (PL) behaviors across the visible and near-infrared (NIR) regions, which has established them as a research focus in the field of advanced functional nanomaterials. This atomic-level precision is specifically reflected in the well-defined "metal core—ligand shell" configuration of ligand-protected gold nanoclusters, which not only provides a structural basis for regulating PL performance but also renders them an ideal model for elucidating the correlation between structure and PL properties. Notably, the PL properties

Kang Li

Kang Li is a PhD candidate at Xiangtan University under the supervision of Prof. Yong Pei. His current research interest is focused on the photoluminescence properties of ligand-protected gold nanoclusters.

Pu Wang

Pu Wang received her PhD from Xiangtan University under the supervision of Prof. Yong Pei, and she joined the chemistry faculty of Xiangtan University in 2018. Her current research interests are focused on the structure, properties, and catalytic applications of gold nanoclusters.

---

[a] *Department of Chemistry, Key Laboratory of Environmentally Friendly Chemistry and Applications of Ministry of Education, Xiangtan University, Hunan Province 411105, China. E-mail: ypei2@xtu.edu.cn; 90wangpu@xtu.edu.cn*

[b] *College of Chemistry & Chemical Engineering, Hunan Normal University, Changsha, Hunan 410081, China*

of ligand-protected gold nanoclusters are highly aligned with the demands of biological applications. Their excellent biocompatibility, relatively low toxicity, and persistent NIR emission capable of penetrating biological tissues render them ideal fluorescent probes for bioimaging, disease diagnostics, and therapeutic applications.[1–7]

However, research on the PL of ligand-protected gold nanoclusters still faces two major challenges. First, from an experimental perspective, although systems with high photoluminescence quantum yield (PLQY) have been synthesized in recent years (*e.g.*, $Ir@Au_{12}$ (PLQY = 87%) and $Au_{16}Cu_6$ (PLQY ≈ 100%)),[8–13] the PLQY of most gold nanoclusters is still relatively low, particularly in the NIR-II region, which fails to meet the signal intensity requirements for practical applications. Second, from a mechanistic perspective, the complex electronic dynamics induced by core–ligand interactions in these gold nanoclusters make it challenging to experimentally determine the origin of PL (core-dominated *vs.* surface-ligand-involved). Furthermore, the strong intrinsic spin–orbit coupling (SOC) of Au atoms efficiently promotes intersystem crossing (ISC) and reverse intersystem crossing (RISC) between singlet and triplet states,[14–16] leading to fluorescence, phosphorescence, thermally activated delayed fluorescence (TADF), and the coexistence of multiple emission phenomena.[17–23] The overlapping emission peaks arising from the small singlet–triplet state energy gap (ΔE_{ST}) further hinder the differentiation of emission types (phosphorescence or TADF).

Recently, experimental studies have made substantial progress in exploring the PL mechanism of ligand-protected gold nanoclusters *via* various characterization techniques, such as steady-state and time-resolved spectroscopy.[18,24,25] These efforts have provided clues to the origin of PL but cannot fully reveal the microscopic mechanisms underlying excited-state dynamics and nonradiative relaxation. First-principles theoretical calculations have become a key tool to address these bottlenecks. Specifically, they can directly overcome the limitations of experimental characterization and provide atomic-level insights for the direct exploration of electronic structures, excited-state relaxation dynamics, and energy/charge transfer processes. With the ongoing advancement of computational methods and the increasing computational efficiency and computing resources, theoretical calculations have become an indispensable partner in experiments, offering theoretical references for the modulation of PL properties in these gold nanoclusters.

Yong Pei

Yong Pei received his bachelor's degree from Xiangtan University in 2001 and his PhD from Nanjing University in 2006. He pursued postdoctoral research at the University of Nebraska-Lincoln from 2006 to 2010. He is now a Professor at Xiangtan University and Hunan Normal University, and his research interests focus on theoretical studies of the structure and optical, catalytic, and electronic properties of coinage metal nanoclusters.

In this review, we summarize the latest experimental advances in enhancing the PL intensity of ligand-protected gold nanoclusters, as well as theoretical studies focused on exploring their excited-state properties. First, we summarize the experimental strategies employed to boost PL efficiency in recent years, including enhancing radiative decay (*e.g.*, heterometal doping) and suppressing nonradiative pathways (*e.g.*, ligand rigidification). Subsequently, we introduce the key computational methods utilized to study the excited-state properties of these gold nanoclusters, including time-dependent density functional theory (TDDFT) and nonadiabatic molecular dynamics (NA-MD), and analyze the applicability and accuracy boundaries of each method. Finally, we discuss theoretical investigations into the excited-state properties of these gold nanoclusters, including the origins of photoluminescence, SOC-driven emission pathways, and excited-state nonradiative relaxation dynamics, aiming to provide theoretical references for the precise design of ligand-protected gold nanoclusters featuring high PL performance.

2. Experimental advances in photoluminescence enhancement

Research on the photoluminescence of ligand-protected gold nanoclusters faces two primary challenges, including low PLQY and unclear photoluminescence mechanisms, which severely constrain the rational design of high-performance gold nanoclusters. Over the past decade, substantial experimental efforts have been devoted to addressing these issues, resulting in a range of effective strategies for PLQY enhancement, including size control,[26–28] heterometallic doping,[8,29–31] tailored ligand engineering,[9,32–34] and aggregation-induced emission (AIE).[35–37] The availability of ligand-protected gold nanoclusters with atomically precise structures and systematic spectroscopic data has also provided an essential experimental foundation for theoretical studies. Such well-defined cluster systems serve as benchmark models for validating computational approaches. For example, in TDDFT calculations, the assessment and selection of exchange–correlation functionals still rely largely on comparisons with experimental optical spectra (see Section 3).

Nevertheless, most existing reviews emphasize synthetic strategies and potential applications of gold nanoclusters with high PLQY, while discussions on how different experimental strategies enhance PLQY *via* photophysical modulation are fragmented across the literature. A unified photophysical framework linking experimental strategies to the key factors that determine PLQY is still lacking. In this context, the present section provides a systematic overview of recent experimental advances in improving the PLQY of ligand-protected gold nanoclusters from a photophysical perspective. By focusing on the key physical parameters governing PLQY, this section highlights major experimental breakthroughs, outlines unresolved challenges, and underscores the indispensable role of computational methods in elucidating PLQY enhancement mechanisms and guiding rational experimental design.

2.1 Photophysical basis for PLQY enhancement

According to the PLQY expression, $\Phi = k_r/(k_r + k_{nr})$, the decay of the excited states in ligand-protected gold clusters proceeds primarily through two competing pathways, *i.e.*, radiative and nonradiative transitions (as illustrated in Fig. 1). The relative magnitudes of the corresponding rate constants ultimately determine the PLQY of the system. Upon photon absorption, an electron is promoted from an occupied orbital to an unoccupied orbital with higher energy, driving the system from the ground state to an excited state. In accordance with Kasha's rule, excitation to higher-lying excited states is typically followed by rapid nonradiative relaxation processes, including internal conversion (IC), ISC, and vibrational relaxation, leading to population of the lowest excited state (S_1 or T_1), from which radiative decay to the ground state mainly occurs. In the radiative process, an excited-state molecule releases energy and returns to the ground state through photon emission. The efficiency of this process is quantified using Einstein's spontaneous emission rate formula:

$$k_r = \frac{\omega^3 e^2}{3\pi\varepsilon_0\hbar c^3}\mu^2 \tag{1}$$

where $\omega = E_{em}/\hbar$ is the angular frequency of the emitted photon, e is the elementary charge, ε_0 is the vacuum permittivity, $\hbar$ is the reduced Planck constant, c is the speed of light in vacuum, and μ is the transition dipole moment.

Within the framework of Einstein's theory of spontaneous emission, both a larger emission energy E_{em} and a larger transition dipole moment μ favor an increased radiative decay rate. Meanwhile, excited states can also return to the ground state through nonradiative pathways. The corresponding nonradiative rate constant k_{nr} is commonly governed by the energy gap law and decreases exponentially with increasing excited–ground state energy gap, which is often correlated with a higher emission energy E_{em}. Consequently, increasing E_{em} not only enhances the radiative transition rate but also suppresses nonradiative decay. Because the equilibrium geometries of the ground and excited states differ, photoexcitation is followed by structural relaxation on the excited-state potential energy surface. This relaxation involves an energetic cost associated with geometric reorganization, which is commonly described by the reorganization energy λ. This relaxation leads to an emission energy E_{em} that is lower than the vertical excitation energy E_{ex} defined at the ground-state equilibrium geometry. Therefore, for a given electronic level structure, suppressing excited-state structural relaxation can reduce energy loss and increase E_{em}. Beyond indirect modulation *via* emission energy, direct control of nonradiative decay channels is also critical. In particular, weakening nonadiabatic coupling between electronic states and reducing electron–vibrational coupling strength can effectively suppress nonradiative processes, thereby lowering k_{nr}.

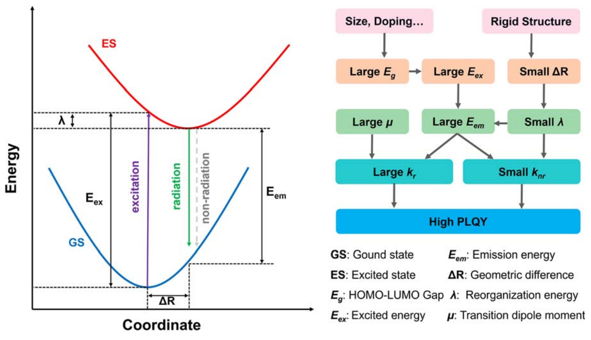

Fig. 1 Schematic illustration of PL processes in ligand-protected gold nanoclusters (left) and the key factors influencing PLQY of ligand-protected gold nanoclusters (right).

In summary, enhancing the PLQY of ligand-protected gold nanoclusters can be achieved by engineering their electronic structures to increase the emission energy and transition dipole moment, while simultaneously suppressing excited-state structural relaxation and nonradiative decay through ligand engineering or structural rigidification. Such strategies enable larger radiative rates and smaller nonradiative rates, ultimately leading to improved photoluminescence efficiency. On this basis, the following sections will systematically review recent experimental efforts aimed at enhancing the PLQY of ligand-protected gold nanoclusters, with particular emphasis on strategies that promote radiative transitions and suppress nonradiative processes.

2.2 Promoting the efficiency of the radiative process

In the radiative process, an excited-state molecule releases energy and returns to the ground state through photon emission. According to Einstein's theory of spontaneous emission, the radiative rate is mainly governed by two key factors: the emission energy E_{em} and the transition dipole moment μ. Accordingly, strategies for enhancing the radiative rate can be broadly classified into two aspects: (i) increasing the emission energy of the lowest excited state through electronic structure modulation, and (ii) enhancing the transition dipole moment to accelerate radiative decay.

2.2.1 Increasing the emission energy. Relative to the ground state, the excitation energy E_{ex}, defined as the energy difference between the excited state and ground state, is determined by the energy gap between occupied and unoccupied orbitals and the electron–hole interaction following excitation. When the lowest excited state (S_1 or T_1) is dominated by a single HOMO → LUMO electronic transition, the excitation energy E_{ex} shows a strong correlation with the HOMO–LUMO gap E_g. In such cases, enlarging E_g through electronic structure modulation is expected to increase the excitation energy of the lowest excited state and increase the emission energy E_{em}. Recently, Buschmann *et al.* summarized the correlations among the HOMO–LUMO gap E_g, the emission energy E_{em}, and the PLQY for a series of Au_{13} core clusters protected by different ligands.[38] Their results revealed that Au_{13} clusters with larger E_g simultaneously exhibit higher emission energies and higher PLQY. These observations provide empirical support for the design strategy of enhancing the emission energy *via* E_g engineering, thereby promoting radiative decay while suppressing nonradiative relaxation.

Previous studies have demonstrated that the HOMO–LUMO gap E_g in ligand-protected gold nanoclusters can be effectively tuned through various experimental strategies, including cluster size control,[39–41] ligand modification,[33,42–44] and metal doping.[8,45,46] Among these strategies, metal doping is an effective strategy to enhance the luminescence efficiency by enlarging the E_g, and it has been widely applied in experiments. Takano and co-workers showed that replacing the central atom of the Au_{13} core with elements lighter than Au (in the order of Au > Pt > Ir in atomic weight) can widen the E_g (Fig. 2A and B).[47] Using this principle, they successfully synthesized a series of heterometal-doped clusters, including $[RuAu_{12}(dppm)_6]^{2+}$, $[RhAu_{12}(dppm)_6]^{3+}$, and $[IrAu_{12}(dppm)_6]^{3+}$ (dppm = 1,2-bis(diphenylphosphino)methane). Notably, $[RuAu_{12}(dppm)_6]^{2+}$ exhibits intense room-temperature phosphorescence in degassed CH_2Cl_2 solution, with a PLQY of 37%.[8] Using a similar doping strategy, a series of clusters with the general formula $[MAu_{12}(dppe)_5Cl_2]$ (M = Au, Pd, Pt, Rh, Ir; dppe = $Ph_2PCH_2CH_2PPh_2$) were also successfully prepared.[30] Experimental results showed that heterometal doping substantially enlarges the E_g of the clusters (Fig. 2B), thereby accelerating radiative transitions while suppressing nonradiative decay pathways. As a result, the PLQY of these systems is significantly enhanced (Fig. 2C). Importantly, such doped cluster systems with well-defined atomic structures and systematic spectroscopic data not only validate the physical mechanism of enhancing radiative efficiency through HOMO–LUMO gap engineering, but also provide ideal experimental models and reliable benchmarks for subsequent excited-state electronic-structure calculations using TDDFT and methodological assessment.

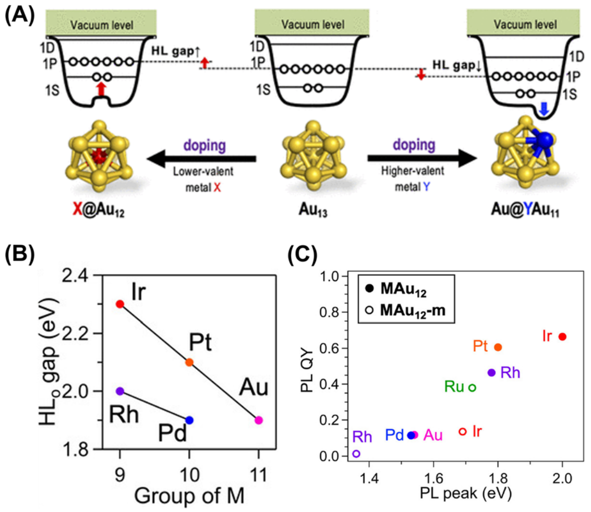

Fig. 2 (A) Two-step jellium potentials for doping lower (left) and higher (right) valent atoms into Au_{13}. Reproduced with permission.[47] Copyright 2021, American Chemical Society. (B) Plot of the HOMO–LUMO gaps of $M@Au_{12}(dppe)_5Cl_2$ (M = Ir, Pt, Au, Rh, Pd). (C) Plot of the PLQYs of $M@Au_{12}(dppe)_5Cl_2$ (MAu_{12}) and $M@Au_{12}(dppm)_6$ (MAu_{12}-m) *versus* the energy of their PL peaks. Reproduced with permission.[30] Copyright 2022, Wiley-VCH.

2.2.2 Increasing the transition dipole moment. In addition to the emission energy E_{em}, the transition dipole moment μ represents another key parameter governing the radiative transition rate. For a given emission energy, excited states with larger transition dipole moments generally exhibit a higher radiative transition rate. Recent studies on the $Au_{38}S_2(S\text{-}Adm)_{20}$ cluster (S-Adm = adamantanethiolate) have shown that this system displays a relatively high PLQY of 15%.[48] The enhanced radiative efficiency was attributed to symmetry-allowed transitions between frontier orbitals (Fig. 3A), which lead to an increase in the transition dipole moment.[48,49] Beyond orbital symmetry, the cluster's overall geometry, specifically its aspect ratio, exerts notable influence on the transition dipole moment. Luo and co-workers reported that a series of rod-shaped Au clusters (Au_{42}, Au_{60}, Au_{78}, Au_{96}, and Au_{114}) with hexagonal close-packed (HCP) cores exhibit unusually intense absorption peaks in their UV-vis spectra[40] (Fig. 3B). Theoretical calculations revealed that these absorption features originate from electronic transitions with large transition dipole moments (Fig. 3C). Among them, the $Au_{42}(PET)_{32}$ cluster (PET = 2-phenylethanethiolate) shows a relatively high PLQY (11.9%),[50] and subsequent theoretical studies by Xie *et al.* confirmed that its large transition dipole moment significantly enhances the radiative decay channel.[51] Similar conclusions have also been supported by computational investigations of Au_{60} clusters.[52] Similarly, in a theoretical study on the optical absorption properties of the $Au_{76}(SR)_{44}$ cluster with a face-centered cubic (FCC) core, Ma *et al.* found that its larger aspect ratio leads to a stronger longitudinal transition dipole moment[53] (Fig. 3D). Although existing studies across different cluster systems have

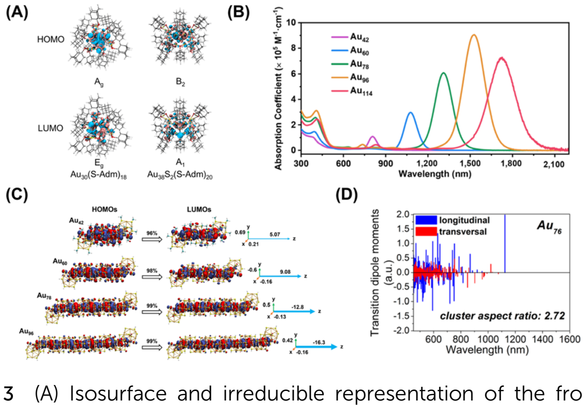

Fig. 3 (A) Isosurface and irreducible representation of the frontier orbitals of $Au_{38}S_2(S\text{-}Adm)_{20}$ and $Au_{30}(S\text{-}Adm)_{18}$. Reproduced with permission.[49] Copyright 2024, American Chemical Society. (B) Optical absorption spectra of Au_{42}, Au_{60}, Au_{78}, Au_{96}, and Au_{114}; (C) the HOMO and LUMO orbitals and electric transition dipole moment for transitions from the ground state to the excited states of $Au_{42}(SCH_3)_{32}$, $Au_{60}(SH)_{44}$, $Au_{78}(SH)_{56}$, and $Au_{96}(SH)_{68}$. Reproduced with permission.[40] Copyright 2024, National Academy of Sciences. (D) Transversal and longitudinal dipole moment transitions of $Au_{76}(SR)_{44}$. Reproduced with permission.[53] Copyright 2016, American Chemical Society.

revealed several empirical correlations between geometric structure, orbital symmetry, and transition dipole moments, a comprehensive understanding of the relationship between the structure of a specific cluster and its transition dipole moment remains to be established.

The HOMO–LUMO gap E_g can be indirectly obtained from experimental techniques such as optical absorption spectroscopy and can be effectively tuned through modulation of cluster size, choice of heterometal dopants, or ligand electronic effects. In contrast, the intensity of an apparent absorption peak in the experimental spectrum may arise from the superposition of multiple excited-state transitions. As a result, it is experimentally challenging to directly correlate the intensity of the longest-wavelength absorption peak with the transition dipole moment of the lowest excited state. Fundamentally, the transition dipole moment is determined by the spatial distribution and symmetry characteristics of the orbitals involved in the electronic transition, which generally require excited-state electronic structure calculations for detailed analysis. This issue becomes particularly important in the context of applications such as bioimaging, where NIR emission is desired and blue-shifting the emission (*i.e.*, increasing the emission energy) is no longer an option. Under such conditions, enhancing the transition dipole moment represents a more viable approach for improving radiative efficiency. Therefore, establishing more general and design-oriented relationships between the cluster structure and transition dipole moment through theoretical calculations is essential for guiding the rational design of highly emissive gold clusters.

2.3 Suppressing nonradiative processes

In addition to radiative transitions, excited-state ligand-protected gold nanoclusters can also undergo nonradiative deactivation pathways, which diminish the PLQY. Consequently, beyond enhancing radiative efficiency, suppressing nonradiative decay channels is another critical strategy for improving the PL performance of gold clusters. In fact, most reported ligand-protected gold nanoclusters still exhibit relatively low PLQY, indicating that nonradiative channels generally dominate the excited-state decay processes.

Structurally, ligand-protected gold nanoclusters adopt a core–shell structure consisting of a metallic core surrounded by an organic ligand shell.[54] In such systems, various vibrational modes introduced by both the metal core and the ligands can couple with electronic excited states, providing efficient pathways for nonradiative energy dissipation. Recent studies have emphasized strategies like ligand shell rigidification and suppression of surface vibrations to mitigate nonradiative relaxation pathways and consequently enhance PLQY.

2.3.1 Ligand rigidification. In ligand-protected gold nanoclusters, increasing the overall rigidity of the ligand shell represents an important strategy for suppressing nonradiative decay. To date, gold clusters protected by various types of ligands have been reported, including thiolates,[55–57] phosphines,[58] alkynyls,[59] and N-heterocyclic carbenes (NHCs).[60,61] By comparing Au_{13} clusters protected by different ligand types, Buschmann *et al.* showed that Au_{13} clusters protected by X-type ligands (*i.e.*, thiolates and alkynyls) typically undergo larger structural relaxation in the excited state, whereas Au_{13} clusters protected by L-type ligands (*i.e.*, phosphines and NHCs) exhibit much smaller excited-state geometric changes.[38]

In recent years, a series of NHC-protected gold clusters with exceptionally high PLQY have been reported. Luo *et al.* synthesized chiral NHC-protected Au_{13} clusters with PLQY as high as 61% (ref. 62) (Fig. 4A). By combining ligand-exchange experiments with theoretical simulations, they revealed that non-covalent inter-ligand interactions, including C–H⋯N, C–H⋯π, and π⋯π interactions, play a crucial role in enhancing the overall rigidity of the ligand shell and suppressing excited-state structural relaxation. Subsequently, Kulkarni *et al.* reported bidentate NHC-protected Au_{13} clusters with PLQY reaching 62% (ref. 10) (Fig. 4B), attributing the enhanced performance to increased ligand rigidity and strong interligand interactions. For diphosphine-protected gold nanoclusters, Mutoh and co-workers combined Ir doping with tailor-made diphosphine ligands to synthesize $[IrAu_{12}(bbpe)_6]^{3+}$ (bbpe = bis[benzo[*b*]phosphindole]ethane), which exhibits an exceptionally high PLQY of 87%.[9] Similar ligand-engineering strategies have also been successfully applied to thiolate-protected gold nanoclusters. Enhancing the π⋯π interactions by reducing the methyl group at the end of the thiol ligand, Wang *et al.* improved the PLQY of the $Au_{52}(SR)_{32}$ cluster from 3.8% to 18.3% (ref. 34) (Fig. 4C). And this approach was subsequently applied to the $Au_{36}(SR)_{24}$ cluster, achieving a similar PLQY enhancement[63] (Fig. 4D).

Collectively, these studies indicate that enhancing inter-ligand interactions to rigidify the ligand shell is an effective strategy for suppressing excited-state structural relaxation and thereby reducing nonradiative decay. However, most ligand-modification approaches reported to date have focused on

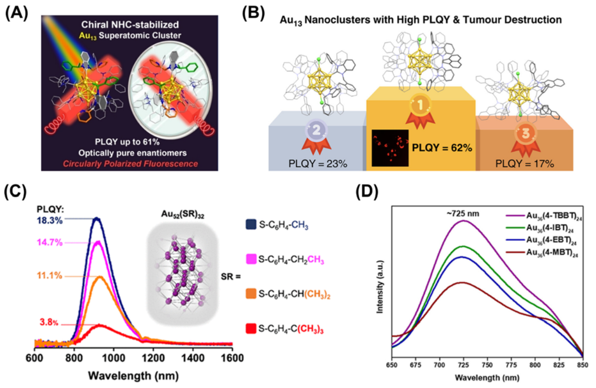

Fig. 4 (A) The chiral NHC-stabilized Au_{13} cluster with high PLQY (61%). Reproduced with permission.[62] Copyright 2023, Wiley-VCH. (B) The bis-NHC-protected Au_{13} clusters with π-extended aromatic systems and high PLQY. Reproduced with permission.[10] Copyright 2025, American Chemical Society. (C) The PLQY of $Au_{52}(SR)_{32}$ with four different aromatic thiolate ligands. Reproduced with permission.[34] Copyright 2023, American Chemical Society. (D) Emission spectra of $Au_{36}(SR)_{24}$ with four different aromatic thiolate ligands. Reproduced with permission.[63] Copyright 2024, American Chemical Society.

hydrophobic ligands. Meanwhile, hydrophilic ligands are essential for ligand-protected gold nanoclusters aimed at biological applications,[4,18,64,65] and the surrounding aqueous environment plays a decisive role in governing their PL properties. From a theoretical perspective, a faithful description of these aqueous environment effects requires going beyond implicit-solvent treatments of bulk polarity and instead adopting explicit, dynamic multiscale simulations (*e.g.*, QM/MM), coupled with nonadiabatic excited-state dynamics to capture solvent-coupled structural relaxation as well as charge- and energy-transfer processes.[66–72] Notably, such multiscale and nonadiabatic approaches have been less frequently applied to ligand-protected gold nanoclusters and merit further development.

2.3.2 Suppression of staple motions. Unlike phosphine and NHC ligands, which bind directly to the metallic core through anchoring atoms (P or C), thiolate ligands in thiolate-protected gold nanoclusters can form characteristic Au–S staple motifs involving a portion of surface gold atoms. The vibrational modes associated with these staple motifs can couple with electronic excited states, thereby facilitating nonradiative energy dissipation. Modulating the Au–S staple structures to restrict their vibrational relaxation has therefore been demonstrated as an effective strategy for enhancing the PLQY of thiolate-protected gold nanoclusters.[73] In 2021, Li *et al.* reported that the $Au_{38}S_2(S\text{-}Adm)_{20}$ cluster exhibited a relatively high PLQY of 15%.[48] They attributed this PL enhancement to the rigidifying effect of surface μ_3-S atoms and eight bridging SR ligands (Fig. 5A), which significantly suppresses energy dissipation caused by Au–S vibration. Similar effects have been further validated in isomeric systems. Chen and Xia *et al.* identified two isomers of $Au_{28}(SR)_{20}$ (Au_{28i} and Au_{28ii}) with identical gold cores but different surface Au–S staple motif structures, leading to significant differences in the PL intensity.[74,75] In particular, the long-lived emission component of Au_{28ii} is significantly enhanced, indicating that the interlocked short motifs effectively inhibit nonradiative decay. Subsequently, Dong *et al.* synthesized the $Au_{28}(SCH_2Ph\text{-}^tBu)_{22}$ cluster, whose compact and rigid shell layer effectively reduced nonradiative energy loss and enhanced the fluorescence intensity.[76]

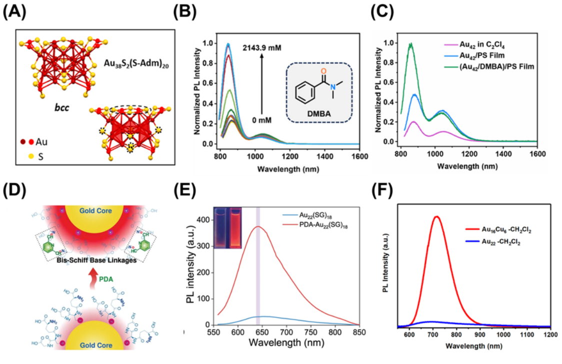

Fig. 5 (A) Atomic structure of $Au_{38}S_2(S\text{-}Adm)_{20}$ determined from single-crystal diffraction. Reproduced with permission.[48] Copyright 2021, American Chemical Society. (B) PLQY of Au_{42} dissolved in deaerated 2-MeTHF containing DMBA (*N*,*N*-dimethylbenzamide) with different concentrations. (C) PL spectra of Au_{42} dissolved in C_2Cl_4 and embedded in a polystyrene (PS) film. Reproduced with permission.[12] Copyright 2024, American Chemical Society. (D) Schematic diagram of intramolecular cross-linking of ligands by the formation of bis-Schiff linkages on the $Au_{22}(SG)_{18}$ surface. (E) PL spectra of $Au_{22}(SG)_{18}$ and PDA-$Au_{22}(SG)_{18}$ NCs. Reproduced with permission.[77] Copyright 2022, Springer Nature. (F) Comparison of the emission spectra of $Au_{16}Cu_6$ and Au_{22} in CH_2Cl_2. Reproduced with permission.[11] Copyright 2024, American Association for the Advancement of Science.

Au–S staple motion can also be constrained through external molecular environments. By introducing amide molecules to further restrict staple vibrations in $Au_{42}(PET)_{32}$ clusters, the room-temperature PLQY was increased to 50% and even reached 75% when embedded in a polymer matrix containing amide molecules[12] (Fig. 5B and C). In addition to environmental confinement, surface modification engineering can achieve similar effects. Deng *et al.* employed bis-Schiff base cross-links to restrict the movement of Au–S staples in individual $Au_{22}(SG)_{18}$ clusters (SG = glutathione), achieving a PLQY of 48% (ref. 77) (Fig. 5D and E). Similar to thiolate-protected systems, alkynyl-protected gold nanoclusters also feature Au–C≡CR staple motifs. Recently, metal doping within staple motifs provides another effective means of suppressing nonradiative decay in alkynyl-protected gold nanoclusters. Shi *et al.* doped six Cu atoms into the surface staple units of $Au_{22}(^tBuPhC{\equiv}C)_{18}$, yielding a more compact $Au_{16}Cu_6(^tBuPhC{\equiv}C)_{18}$ cluster with a near-unity PLQY approaching 100% (ref. 11) (Fig. 5F). From a theoretical perspective, suppressing staple vibrations can be viewed as mitigating excited-state structural relaxation and vibronic coupling at the surface, thereby reducing nonradiative decay.

In summary, experimental studies on the photoluminescence of ligand-protected gold nanoclusters in recent years have established a clear and reproducible set of structure–property relationships. Although the specific experimental strategies differ in their practical implementations, their underlying mechanisms can be consistently rationalized in terms of effective modulation of key parameters governing excited-state decay processes. On the one hand, radiative decay rates are enhanced by increasing the emission energy and the transition dipole moment. On the other hand, nonradiative decay is efficiently suppressed by strengthening the rigidity of ligands and surface motifs and by reducing the coupling between vibrational modes and electronic excited states.

It should be emphasized that these experimental observations cannot be fully understood solely on the basis of static structural parameters or ground-state electronic structures. Instead, they critically depend on excited-state electronic structure characteristics, including energy levels, coupling parameters, and the dynamical evolution of excited-state decay processes. Therefore, to achieve a systematic mechanistic understanding and predictive capability for the PLQY of ligand-protected gold nanoclusters, it is essential to introduce theoretical and computational frameworks centered on excited states. Beyond identifying the key factors governing PLQY, theoretical methods are also indispensable for determining emission types, elucidating emission origins, and describing the dynamics of nonradiative relaxation processes. This includes not only calculations of excited-state energies and transition properties based on TDDFT, but also quantitative descriptions of SOC effects, ISC, and vibrational coupling accompanied by structural relaxation. On this basis, the following section will focus on the crucial role of excited-state theoretical approaches in addressing these issues.

3. Theoretical tools for understanding photoluminescence

Although extensive experimental efforts have been devoted to enhancing the PLQY of ligand-protected gold nanoclusters and to elucidating their excited-state properties and emission pathways,[18,19,24,31,41] there is still a lack of a comprehensive understanding of their PL mechanisms, which hinders the rational design of clusters with specific emission wavelengths and lifetimes. Specifically, experimental characterization faces three limitations. Firstly, the origin of photoluminescence remains ambiguous due to the inherent core–shell structure of ligand-protected gold nanoclusters. Experimental researchers have proposed several competing explanations, including core-dominated emission, ligand participation, ligand-to-metal charge transfer (LMCT), and metal-to-ligand charge transfer (MLCT). These hypotheses remain under debate because the electronic distribution and transfer processes in the excited states of the clusters cannot be directly observed. Secondly, the strong SOC in gold atoms often results in the coexistence of multiple emission types, including fluorescence, phosphorescence, and TADF. However, the experimentally observed fluorescence and phosphorescence emission bands usually overlap owing to their broad bandwidths and small energy separations, making it challenging to unambiguously distinguish and assign the emission types. Finally, although ultrafast spectroscopy provides powerful means to probe the timescales of excited-state relaxation in these clusters, capturing the atomic-scale details of processes such as structural relaxation (*e.g.*, core distortion and ligand vibration) and charge or energy transfer remains highly challenging.

Theoretical calculations can complement these experimental limitations and serve as indispensable tools for elucidating PL mechanisms. In light of the challenges mentioned above, this section systematically reviews two major computational approaches employed to investigate the PL mechanisms of ligand-protected gold nanoclusters and clarifies their relevance to the unresolved experimental issues (as illustrated in Fig. 6). The first category involves electronic structure methods, including density functional theory (DFT), TDDFT, and multi-configurational methods. By selecting an appropriate theoretical methods, theoretical calculations can reproduce experimental absorption and emission spectra, thereby providing a reliable foundation for subsequent rate-constant evaluations and excited-state property analyses. In particular, analytical tools such as natural transition orbital (NTO) and electron–hole analysis[78] enable direct visualization of charge distribution and transfer characteristics in excited states, helping to elucidate the origin of photoluminescence. The second category focuses on the simulation of nonradiative processes, encompassing static rate-constant calculations based on Fermi's golden rule and NA-MD methods that explicitly account for electron–nuclear coupling. By computing and comparing rate constants associated with different decay pathways, one can distinguish emission types, estimate PLQY, and unravel the underlying mechanisms. Moreover, NA-MD simulations provide time-resolved insights into electronic relaxation dynamics, revealing transition times and pathways among excited states. Together, these computational strategies establish a robust methodological framework for in-depth mechanistic analysis of photoluminescence and for the rational design of ligand-protected gold nanoclusters with enhanced PL performance.

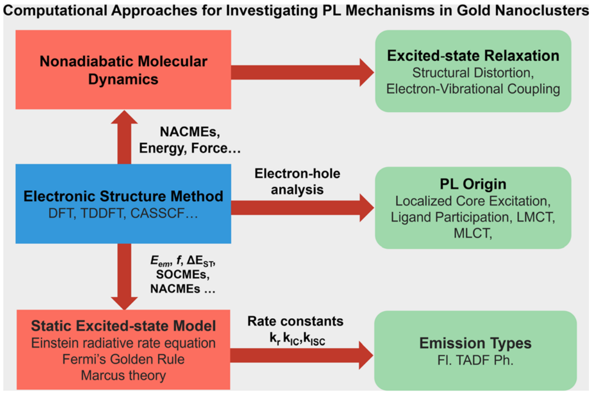

Fig. 6 Computational approaches for investigating PL mechanisms in ligand-protected gold nanoclusters.

3.1 Electronic structure methods

The selection of electronic structure methods is pivotal for accurately modeling the electronic configuration and deriving dependable photophysical characteristics, serving as a fundamental prerequisite for valid theoretical interpretations. DFT and TDDFT are widely used to analyze the electronic structure and excited-state properties of ligand-protected gold nanoclusters, owing to their favorable balance between computational efficiency and accuracy.[43,55,79,80] However, the reliability of theoretical predictions, such as UV-vis absorption spectra, emission energies, and excited-state lifetimes, strongly depends on the choice of the exchange–correlation functional.[80–83]

Generalized gradient approximation (GGA) functionals, such as BP86 (ref. 84) and PBE,[85] are frequently selected in computational studies of ligand-protected gold nanoclusters due to their computational efficiency and acceptable accuracy. However, they tend to underestimate excitation energies, thus limiting their applicability in excited-state properties. Recently, in the computational investigation of X@Cu_{14} (X = Au, Cl) clusters, Luo *et al.* assessed the performance of three GGA/meta-GGA functionals (BP86, PBE, and TPSS[86,87]) and nine hybrid functionals (PBE0,[88] B3LYP,[89,90] revPBE38,[91] TPSSh,[92] TPSS0,[93] M06, M06-2X,[94] CAM-B3LYP,[95] and ωB97X-D4 (ref. 96)) for the calculation of fluorescence and phosphorescence emission energies.[97] For Au@Cu_{14}, hybrid functionals with high Hartree–

Fock exchange (*e.g.*, revPBE38) most accurately replicate the experimental $T_1 \rightarrow S_0$ phosphorescence emission energy (Fig. 7), while for $Cl@Cu_{14}$, GGA/meta-GGA functionals (BP86, PBE, and TPSS) align more closely with the experiment. Notably, the calculated $\Delta E(S_1–T_1)$ increased with higher HF exchange fractions, resulting in a growing deviation between the calculated fluorescence and phosphorescence emission properties and experimental data. Additionally, the oscillator strengths of fluorescence radiation show an increasing trend with rising HF exchange percentage in the functional. For phosphorescence radiation, except for M06-2X, other functionals showed minimal influence on the oscillator strengths. Qian and co-workers evaluated the performance of various functionals for ligand-protected noble-metal clusters, finding that the proportion of HF exchange predominantly influences simulated spectral features, regardless of the hybrid functional type.[98] Benchmarking against experimental spectra indicates that functionals incorporating approximately 10–20% HF exchange yield the most accurate spectral predictions. Furthermore, She *et al.* examined the fluorescence mechanisms and doping effects in heteroatom-doped $M@Au_{12}(dppe)_6{}^{x-2}$ clusters, with M representing a 4d or 5d transition metal, and *x* denoting the nominal charge. They benchmarked several exchange–correlation functionals by comparing the calculated optical absorption and fluorescence spectra of $[Au_{13}(dppe)_5Cl_2]^{3+}$ with experimental data.[79] They found that the PBE functional markedly underestimates emission energies, while HSE06 (ref. 99) offers the best consistency with experimental observations. Taken together, these studies indicate that no universal exchange–correlation functional has yet been established for ligand-protected gold nanoclusters. The optimal choice remains system-dependent and typically requires benchmarking against experimental spectra or higher-level calculations.

In theoretical calculations, electronic excitation properties (such as local and charge-transfer excitations) can be characterized using NTO or hole–electron analysis. Specifically, such analyses are performed to calculate the excited-state properties of clusters *via* DFT and TDDFT methods combined with optimal exchange–correlation functionals, to further obtain the orbital compositions and transition contributions of the excited-state electronic structure, and ultimately to quantitatively determine the respective contributions of the metal core and ligand shell in the excited-state transitions, thereby elucidating the origin of photoluminescence. For instance, Weerawardene *et al.* utilized TDDFT to study $Au_{25}(SR)_{18}{}^{-}$ clusters and revealed that the emission primarily originates from core-based transitions (*i.e.*, excitations out of superatom P orbitals into the lowest two superatom D orbitals).[100]

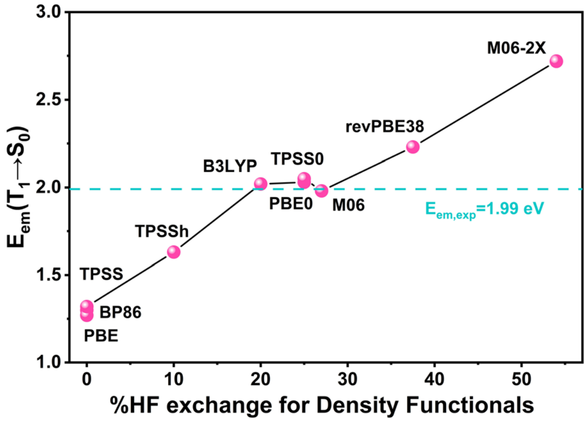

Fig. 7 Calculated $T_1 \rightarrow S_0$ emission energies of $Au@Cu_{14}$ using functionals with different fractions of Hartree–Fock exchange.

While DFT and TDDFT provide an advantageous compromise between computational efficiency and accuracy, their computational cost escalates rapidly as the size of gold nanoclusters (*e.g.*, beyond Au_{50}) increases, limiting the feasibility of simulating larger systems. Concurrently, the electronic and steric influences of protecting ligands markedly affect the photophysical characteristics of gold nanoclusters.[9,34,79] This presents a methodological challenge: simplifying ligand structures to reduce computational demand introduces systematic discrepancies, whereas employing realistic ligand models substantially elevates computational resource requirements. In their study of the dual-emission mechanism of the $Au_{14}Cd(S\text{-}Adm)_{12}$ cluster,[101] Havenridge and co-workers observed that the absorption spectra are highly sensitive to ligands. Simplifying ligands, such as substituting Adm groups with hydrogen or methyl groups, may lead to deviations from the authentic photophysical responses of the actual system. They thus applied a combined approach of TDDFT and tight-binding approximation (TDDFT + TB)[102] to simulate absorption spectra of $Au_{14}Cd(S\text{-}Adm)_{12}$ protected by full ligands. This approach yielded computational efficiency comparable to that of TDDFT while significantly reducing computational effort. Subsequently, they developed an innovative approximation method, termed TDDFT-aas (time-dependent density functional theory approximate auxiliary s-function), which does not depend on tight-binding parameters.[103] Within higher computational efficiency, the calculated absorption spectra of silver and gold nanoparticles using the TDDFT-aas method are in good agreement with the results of TDDFT and TDDFT + TB. Furthermore, the implementation of analytical excited-state gradients within the TDDFT-aas framework facilitates efficient calculation of emission energies for larger nanoclusters.

It is worth noting that TDDFT may struggle to accurately describe potential energy surfaces near conical intersections or state crossings, where multi-configurational methods (*e.g.*, CASSCF) become essential. In 2016, Wu *et al.* investigated the photoluminescence mechanisms of ultrasmall ligand-protected gold nanoclusters using the CASPT2//CASSCF approach, which enabled highly accurate predictions of absorption and emission wavelengths in excellent agreement with experimental data.[104] For example, when applied to the cluster $[Au_7(dppp)_4]^{3+}$ (dppp = 1,3-bis(diphenylphosphino)propane), the calculated phosphorescence emission energy was 644 nm, matching the experimental value (642 nm) with a deviation of only 2 nm. However, the high computational cost and the need for careful active-space selection limit the applicability of multi-configurational methods to larger or more complex systems.[105]

3.2 Simulation of nonradiative processes

The PLQY of ligand-protected gold nanoclusters is determined by the competition between radiative and nonradiative decay pathways, serving as a critical parameter for evaluating their photoluminescence efficiency. However, experimental approaches often face challenges in directly resolving the microscopic mechanisms of nonradiative relaxation processes (such as excited-state structural relaxation and electron-nuclear coupling interactions) and in quantitatively assessing their influence on PLQY. Consequently, theoretical calculations become essential for providing deeper mechanistic insight. To theoretically determine the PLQY value, the primary goal is to calculate the radiative rate constant k_r and the nonradiative rate constant k_{nr},[106–108] which in turn allows for a clear determination of the reasons behind low PLQY. Notably, early theoretical studies of ligand-protected gold nanoclusters focused primarily on their absorption and emission spectra, oscillator strengths, emission energies, and radiative rate constants.

The radiative rate constant k_r is predominantly determined using Einstein's spontaneous emission rate expression (eqn (1)), which requires prior calculation of the emission energy and transition dipole moment through methods such as TDDFT. In contrast, modeling nonradiative processes remains a significant challenge in theoretical chemistry and is critical for accurately predicting the PLQY of ligand-protected gold nanoclusters. According to the energy gap law,[109] the IC rate constant k_{IC} increases exponentially as the emission energy E_{em} decreases, which can be expressed as $k_{IC} = Ae^{-\alpha E_{em}}$. However, since vibronic coupling phenomena between electronic states are not explicitly incorporated, this empirical expression provides only a rough estimate and has limited applicability. Additionally, the strong relativistic effect in gold atoms induces significant SOC, which facilitates ISC from singlet to triplet states. Consequently, ligand-protected gold nanoclusters can exhibit phosphorescence, TADF, or dual emission[17–23,50] involving triplet states and the associated ISC and RISC processes. Therefore, a thorough analysis of both ISC and RISC pathways is essential for understanding the luminescence properties and mechanisms of these nanoclusters. Typically, ΔE_{ST} and spin–orbit coupling matrix elements (SOCMEs) are utilized to estimate the competition between ISC and RISC *via* Fermi's golden rule, thereby helping to identify the emission type of ligand-protected gold nanoclusters. Furthermore, direct evaluation of ISC rate constant k_{ISC} and RISC rate constant k_{RISC}, and their comparison with k_r and IC rate constant k_{IC}, enables comprehensive mapping of excited-state decay pathways and facilitates quantitative prediction of excited-state lifetimes and PLQY.[106]

However, nonradiative processes, such as IC, ISC, and RISC, involve intricate couplings among electronic and nuclear degrees of freedom,[110,111] making accurate theoretical treatment particularly challenging. According to Fermi's golden rule, the nonradiative transition rate constant k_{nr} governing transitions between two electronic states can be expressed as follows:

$$k_{nr} = \frac{2\pi}{\hbar}\left|\left\langle \Psi_f \middle| \hat{H}' \middle| \Psi_i \right\rangle\right|^2 \rho(\Delta E) \tag{2}$$

where $\langle \Psi_f | \hat{H}' | \Psi_i \rangle$ represents the nonadiabatic coupling (NAC) Hamiltonian (for IC) or the SOC Hamiltonian (for ISC) between the initial state i and the final state f, $\hbar$ is the reduced Planck constant, and $\rho(\Delta E)$ is the vibrational density of states at the energy gap ΔE.

Recent advances by Shuai,[107,112] Marian,[113,114] Santoro,[115] Valiev[116] and others have established general rate-constant formulations that incorporate vibrational overlap and the Duschinsky rotation effect, which have been implemented in computational packages for evaluating nonradiative rate constants. For instance, Xie *et al.*[51] applied Lin's formalism[117,118] to compute the ISC and RISC rate constants (6.87×10^7 s^{-1} and 2.87×10^2 s^{-1}, respectively). By combining these with the fluorescence and phosphorescence radiative rate constants (1.53×10^8 s^{-1} and 8.52×10^3 s^{-1}, respectively), they provided a theoretical explanation of the dual-emission behavior observed in the $Au_{42}(PET)_{32}$ cluster. Recently, Li *et al.* computed nonradiative rate constants for $Au_{38}S_2(SR)_{20}$ and $Au_{30}(SR)_{18}$ with the FCclasses3 program.[49] Based on the computed rate constants and the law of mass action, exciton population evolution diagrams were subsequently constructed to analyze the excited-state decay pathways and emission characteristics of these clusters. In addition to rate-constant calculations, analyses of the Huang–Rhys factors and reorganization energies, which were decomposed into contributions from individual vibrational normal modes, provided further insight into how cluster structure influences nonradiative decay processes. However, the excited-state lifetimes and PLQYs predicted by the current methods tend to be significantly lower than experimental values, primarily due to the neglect of anharmonic vibrational effects.[108,116,119,120] Moreover, these Fermi's golden rule-based approaches require the computation of excited-state vibrational frequencies, which becomes computationally prohibitive for larger clusters. As a practical alternative to Fermi's golden rule-based approaches, Marcus theory has been employed to estimate the ISC and RISC rate constants:[121–124]

$$k_{ISC(RISC)} = \frac{2\pi}{\hbar} V_{SOC}{}^2 \frac{1}{\sqrt{4\pi\lambda\kappa_B T}} \exp\left[-\frac{(\Delta E_{ST} + \lambda)^2}{4\lambda\kappa_B T}\right] \tag{3}$$

where ΔE_{ST} is the adiabatic energy difference between the S_1 and T_n states. k_B is the Boltzmann constant and T is the thermodynamic temperature. V_{SOC} is the spin–orbit coupling matrix element (SOCME), and λ is the reorganization energy.

Beyond the static excited-state decay models based on Fermi's golden rule discussed above, nonadiabatic molecular dynamics (NA-MD) has emerged as a powerful tool for elucidating the ultrafast excited-state relaxation pathways of ligand-protected gold nanoclusters.[125,126] NA-MD simulations can provide detailed information on the electronic relaxation dynamics, including state-to-state transition times and mechanisms. For instance, NA-MD simulations of the $Au_{25}(SR)_{18}{}^-$ cluster revealed that the experimentally observed picosecond-scale processes likely originate from core-to-core transitions rather than the previously proposed core-to-half-ring transitions.[102] However, most current NA-MD studies of ligand-protected gold nanoclusters neglect SOC effects, thereby omitting ISC between singlet and triplet states. For ligand-protected gold nanoclusters, reproducing ISC processes that accompany dynamical structural transformations within NA-MD remains highly challenging. This difficulty primarily arises from the need to compute triplet-state energy levels and SOCMEs along nuclear trajectories. Additionally, earlier nonadiabatic simulations of nanoclusters primarily relied on the independent-particle approximation, in which excited states are represented as single-particle excitations constructed from Kohn–Sham orbitals. Within this framework, the state energies and nonadiabatic couplings (NACs) are evaluated using single Slater determinants, thereby neglecting critical carrier–carrier interactions. Recently, Xie and co-workers[127] compared simulation results obtained from both single-particle and many-body (MB) treatments in their NA-MD study of $Au_{25}(SR)_{18}^-$. Their findings demonstrated that the inclusion of MB effects significantly enhanced the NAC between excited states, resulting in ultrafast IC from higher excited states on a sub-picosecond timescale, which is consistent with previous experimental observations. Future developments of NA-MD simulation methods in ligand-protected gold nanoclusters need to incorporate relativistic effects, ISC processes, and carrier–carrier interactions to more accurately reproduce the excited-state dynamics of ligand-protected gold nanoclusters.[71,72,127–129]

4. Mechanistic insights into photoluminescence and excited-state dynamics

Section 3 has already systematically introduced the applicability logic of core methods such as DFT, TDDFT, and NA-MD in the study of ligand-protected gold nanoclusters. Therefore, this section will adopt a "Computational Method → Mechanism Elucidation" framework to systematically summarize the current theoretical research status concerning the photoluminescence origin, excited-state relaxation dynamics, and emission mechanisms, using case studies from typical cluster systems. This summary will explicitly define the core role of different computational methods in elucidating these mechanisms, thereby providing a valuable reference for subsequent theoretical studies and rational structure design.

4.1 Origin of photoluminescence

The core–shell structure of ligand-protected gold nanoclusters, consisting of a metal core and a ligand shell (as illustrated in Fig. 8), gives rise to diverse PL origins, including core-dominated emission, ligand-involved emission, and charge-transfer processes such as LMCT and MLCT. In some systems, structural relaxation and nonradiative processes (IC or ISC) can reshape the character of the excited state, enabling conversion between initially populated charge-transfer states and a core-dominated excitation state before emission. Furthermore, the intricate interactions between the metal core and ligand shell lead to complex excited-state properties and electronic dynamics, which make experimental identification of the PL origin highly challenging. TDDFT, combined with NTO analysis or electron–hole analysis, has thus emerged as a powerful tool for clarifying excited-state electronic behavior. This method serves as an important tool for elucidating the dominant PL origin and understanding the structural factors that modulate emission by enabling direct comparison among different cluster systems. At present, research on the PL origin in ligand-protected gold nanoclusters can be broadly classified into two major categories.

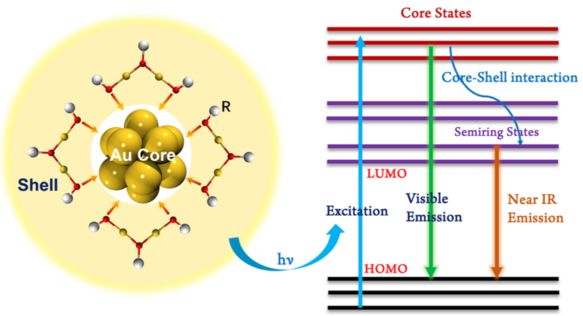

Fig. 8 The photoluminescence origin diagram of ligand-protected gold nanoclusters.

(1) Core-dominated excitation: for the majority of ligand-protected gold nanoclusters, PL originates primarily from core-localized electronic excitation. In this case, the emission is governed by electronic transitions within the metal core, whereas the ligands mainly modulate the orbital energy levels through electron-donating or -withdrawing effects and influence core structural relaxation *via* steric hindrance. This conclusion has been consistently validated across multiple systems using TDDFT calculations. For example, early transient absorption spectroscopy (TAS) studies on the $Au_{25}(SR)_{18}^-$ cluster suggested that its PL might arise from ligand–metal, charge-transfer, or semi-ring states.[130] To resolve this controversy, Weerawardene *et al.* employed TDDFT to calculate the excited-state electronic structures of $Au_{25}(SR)_{18}^-$ clusters clearly modified with different R groups ($R = H, CH_3, C_2H_5, C_3H_7$).[100] Their results clearly demonstrated that the emission originates predominantly from core-based transitions rather than charge-transfer or semi-ring states (Fig. 9A), thereby providing a theoretical resolution to the long-standing debate over this system's emission origin. Subsequent TDDFT calculations on systems such as $Au_{38}(SR)_{24}$,[131] $Au@Cu_{14}$,[97] $Au_{22}(C{\equiv}CR)_{18}$,[132] $Au_{42}(PET)_{32}$ (Fig. 9B),[52] and $Au_{38}S_2(S\text{-}Adm)_{20}$ (ref. 49) further confirmed the dominance of core-localized excitation. Furthermore, Weerawardene *et al.*[100] illustrated the ligand-dependent modulation of emission energy for $Au_{25}(SH)_{18}^-$, $Au_{25}(SCH_3)_{18}^-$, and $Au_{25}(SCH_2CH_2CH_3)_{18}^-$, and the fluorescence emission energies were calculated to be 0.829 eV, 0.655 eV, and 0.512 eV, respectively.

(2) Charge transfer: in contrast, for certain Au(I) clusters and specific ligand-protected systems, the ligands participate directly in electronic transitions, giving rise to LMCT. For instance, studies on the PL properties of Au(I) and Cu(I) clusters protected by NHC ligands,[133] which exhibit highly efficient TADF, revealed through NTO analysis that the S_1 state in all clusters displayed LMCT characteristics. Similarly, in the Cl-

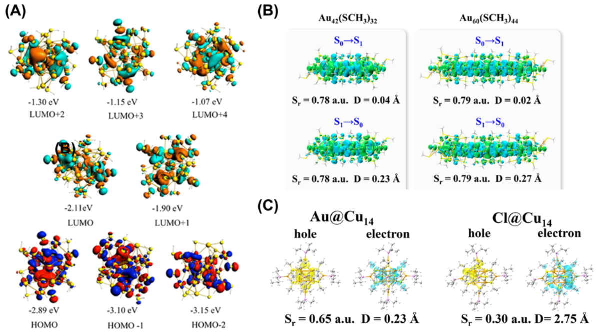

Fig. 9 (A) Kohn–Sham orbitals and orbital energies for the S_1 state of $Au_{25}(SH)_{18}^-$. Reproduced with permission.[94] Copyright 2016, American Chemical Society. (B) Distributions of hole and electron pairs during the electronic transitions of Au_{42} and Au_{60} (blue regions represent holes and green regions represent electrons). Reproduced with permission.[53] Copyright 2025, American Chemical Society. (C) Distribution of hole and electron pairs during the $T_1 \rightarrow S_0$ transition at the optimized T_1 geometry of $Au@Cu_{14}$ and $Cl@Cu_{14}$. Reproduced with permission.[91] Copyright 2025, American Chemical Society.

doped $Cl@Cu_{14}$ cluster, the T_1 state exhibits charge-transfer features (Fig. 9C),[97] whereas the PL origin in the $Au@Cu_{14}$ system remains core-localized excitation. Furthermore, He *et al.* demonstrated that Au doping in $AuAg_{12}$ and Au_3Ag_{10} induces significant charge-transfer characteristics.[134]

4.2 SOC and emission pathways

Ligand-protected gold nanoclusters, which comprise several tens of gold atoms or more, exhibit pronounced SOC owing to the heavy-atom effect of gold. Serving as a pivotal mediato, SOC accelerates ISC between singlet and triplet states and, by regulating the RISC rate, directly dictates the emission pathway, namely fluorescence, phosphorescence, or TADF (Fig. 10 left). Early studies often overlooked SOC and the associated ISC/RISC processes, which obscured the interpretation of complex photoluminescence behaviors. Here, we summarize advances in elucidating emission types of ligand-protected gold nanoclusters based on quantitative rate-constant calculations and analyses, with particular emphasis on how SOC is incorporated into the models. By computing ISC and RISC rate constants, we clarify the determinative roles of SOC and the ΔE_{ST} in selecting the final emission channel, thereby establishing a "Structural Factors → SOC Effects → Emission Type" regulatory framework (Fig. 10 right).

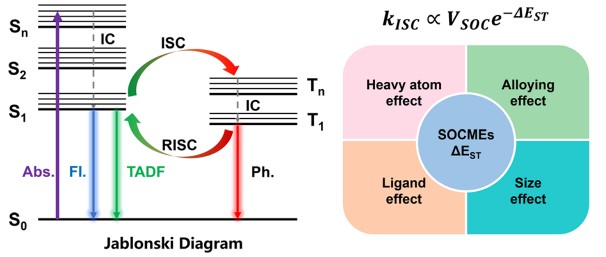

Fig. 10 Jablonski diagram of fluorescence, TADF, and phosphorescence emission processes (left), and factors influencing ISC and RISC processes (right).

4.2.1 Influence of SOC and ΔE_{ST} on emission types.

The SOC effect operates chiefly by opening the phosphorescent radiative pathway and by setting the emission outcome through competition between ISC and RISC. This competition is governed by two key parameters: the ΔE_{ST} and the SOCMEs. A smaller ΔE_{ST} facilitates RISC and favors TADF, whereas a larger ΔE_{ST} suppresses RISC and favors phosphorescence. Larger SOCMEs enhance ISC efficiency and increase the phosphorescent radiative rate. The interplay between ΔE_{ST} and SOCMEs can therefore yield multiple emission types and even dual-emission behavior. This mechanism should be validated with multi-state model simulations and quantitative rate calculations.

(1) Differences of emission in isomers: in 2020, the groups of Jin and Wu independently reported two isomeric $Au_{28}(SR)_{20}$ clusters (*i.e.*, $Au_{28i}(SR)_{20}$ and $Au_{28ii}(SR)_{20}$).[74,75] Although both possess an identical Au_{14} core, differences in their ligand-staple motifs led to markedly different PLQYs. An earlier DFT/TDDFT study by Li *et al.*[135] proposed an anti-Kasha S_2 fluorescence mechanism but did not incorporate SOC effects or triplet states. More recently, Mazumder *et al.* combined temperature and oxygen quenching experiments with calculations of ISC and RISC rate constants,[20] revealing the emission type and PL mechanism of two $Au_{28}(SR)_{20}$ isomers (Fig. 11A). $Au_{28i}(SR)_{20}$ exhibited a small ΔE_{ST} (0.126 eV), resulting in comparable $T_1 \rightarrow S_1$ RISC and $S_1 \rightarrow T_1$ ISC rate constants (2.90×10^{10} s^{-1} and 3.53×10^{10} s^{-1}, respectively), thus showing both phosphorescence and TADF. In contrast, $Au_{28ii}(SR)_{20}$ has a larger ΔE_{ST} (0.240 eV), which suppresses RISC (9.87×10^3 s^{-1}) and leads exclusively to phosphorescence *via* the ISC pathway. Furthermore, rate constant calculations also indicated that the higher-lying T_2 state provides an indirect and efficient nonradiative channel from the excited singlet states to the triplet states, reinforcing the conclusion that SOC directly regulates the emission type.

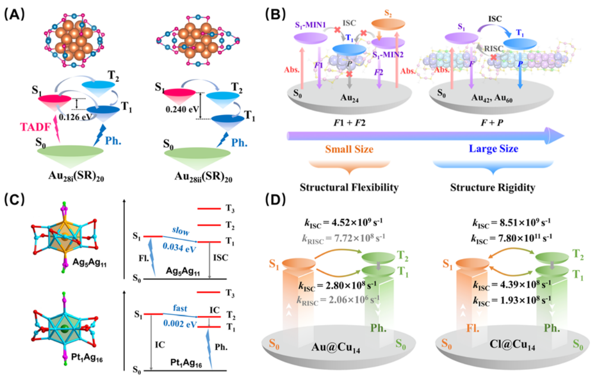

Fig. 11 Simulated mechanism of photoluminescence for (A) $Au_{28i}(SR)_{20}$ and $Au_{28ii}(SR)_{20}$. Reproduced with permission.[20] Copyright 2024, American Chemical Society. (B) Au_{24}, Au_{42}, and Au_{60} clusters. Reproduced with permission.[52] Copyright 2025, American Chemical Society. (C) Au_5Ag_{11} and Pt_1Ag_{16}. Reproduced with permission.[136] Copyright 2022, Wiley-VCH. (D) $Au@Cu_{14}$ and $Cl@Cu_{14}$. Reproduced with permission.[97] Copyright 2025, American Chemical Society.

(2) Three-state modeling of dual emission mechanism: to rationalize the dual emission of $Au_{42}(PET)_{32}$, Xie *et al.* established a three-state kinetic model (S_1, T_1, and S_0) and simulated the ISC and RISC processes.[51] Because S_1 and T_1 share similar localized electronic character, the SOCME between S_1 and T_1 is relatively weak ($46.49\ cm^{-1}$), consistent with the El-Sayed rule. In addition, the S_1 state has a large oscillator strength, yielding a high fluorescence radiative rate constant ($1.53 \times 10^8\ s^{-1}$) that is comparable to the relatively modest $S_1 \rightarrow T_1$ ISC rate constant ($6.87 \times 10^7\ s^{-1}$). Consequently, a fraction of excitons return directly to S_0 *via* fluorescence, while the remainder populate T_1 through $S_1 \rightarrow T_1$ ISC. From T_1, the subsequent phosphorescence rate ($8.52 \times 10^3\ s^{-1}$) substantially exceeds the RISC rate ($2.87 \times 10^2\ s^{-1}$), producing phosphorescence. Overall, the competition among these sequential pathways accounts for the coexistence of fluorescence and phosphorescence in $Au_{42}(PET)_{32}$.

4.2.2 Modulation of SOC and ΔE_{ST}. Structural factors within a nanocluster, such as central-atom doping, ligand modification, and alloying, tune the spin–orbit landscape by modulating the SOCMEs and the ΔE_{ST} (Fig. 10 right). They shift the ISC/RISC balance and enable control over the emission channel, including fluorescence, phosphorescence, and TADF.

(1) Heavy-atom effect of core atom doping: a comparison of calculations between $Au@Cu_{14}$ and $Cl@Cu_{14}$ clearly illustrates the mechanism of heavy-atom regulation effect (Fig. 11D).[97] Owing to the incorporated Au, $Au@Cu_{14}$ shows a substantially larger SOCME value ($2.17\ cm^{-1}$) compared to that of $Cl@Cu_{14}$ ($0.77\ cm^{-1}$). This stronger SOC, together with a smaller $\Delta E_{ST}(S_1–T_2)$ of 0.03 eV, results in a faster $S_1 \rightarrow T_2$ ISC rate ($1.58 \times 10^{10}\ s^{-1}$). As a result, $Au@Cu_{14}$ exhibits strong phosphorescence (PLQY = 71.3%) *via* the $S_1 \rightarrow T_2 \rightarrow T_1 \rightarrow S_0$ pathway. In contrast, the weaker SOC in $Cl@Cu_{14}$ leads to competition between ISC and RISC among S_1, T_1, and T_2, producing the coexistence of TADF and phosphorescence. This comparison clarifies the enhancing role of heavy-atom doping in strengthening SOC.

(2) Alloying effects: to investigate how doping concentration influences emission, He *et al.* performed theoretical calculations on Ag_{13}, Au_{13}, and the model alloy clusters $AuAg_{12}$ and Au_3Ag_{10}, all of which share the identical icosahedral core structure and superatom electronic configuration ($1S^21P^6$).[134] For Au_{13}, which exhibits strong NIR emission, the large $T_2–T_1$ energy gap (0.55 eV) allows T_2 phosphorescence to compete effectively with the $T_2 \rightarrow T_1$ IC process, indicating that its emission primarily originates from the $T_2 \rightarrow S_0$ transition. In contrast to the localized S_1 and T_1 states found in Au_{13} and Ag_{13}, the T_1 state in $AuAg_{12}$ and Au_3Ag_{10} exhibits pronounced charge-transfer character induced by Au doping (Fig. 12). This modification enhances the SOCMEs ($23.97\ cm^{-1}$ for $AuAg_{12}$ and $45.55\ cm^{-1}$ for Au_3Ag_{10}) and reduces the ΔE_{ST} relative to Ag_{13} (about 0.01 eV for $AuAg_{12}$ and 0.03 eV for Au_3Ag_{10}). These effects accelerate ISC and increase the overall PLQY.

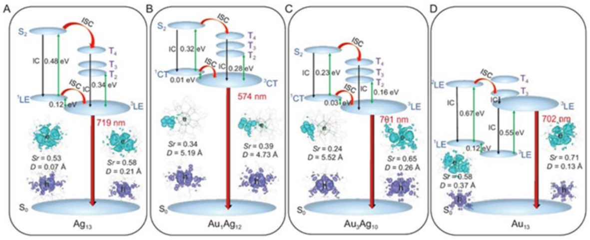

Fig. 12 Energy diagrams and images of the hole and electron pairs of (A) Ag_{13}, (B) Au_1Ag_{12}, (C) Au_3Ag_{10} and (D) Au_{13}. The S_r index is defined as the full space integration of a function ($S_r(r)$) describing the overlap between electron and hole distributions, and the D index is the distance between a hole and an the electron center of mass. Reproduced with permission.[134] Copyright 2024, Oxford University Press on behalf of the Chinese Academy of Sciences.

Investigation into the analogous dopant effects of various metals on photoluminescence has also been conducted for Au_5Ag_{11} (fluorescence) and Pt_1Ag_{16} (phosphorescence).[136] The computational analysis revealed the photoluminescence mechanisms of Au_5Ag_{11} and $PtAg_{16}$ (Fig. 11C). For Au_5Ag_{11}, only the T_1 state lies below the S_1 state, with a relatively larger ΔE_{ST} between S_1 and T_1 (0.034 eV) than that of Pt_1Ag_{16} (the ΔE_{ST} between S_1 and T_2 is about 0.002 eV), resulting in a small ISC rate constant that favors radiative emission as fluorescence. In contrast, in Pt_1Ag_{16}, the S_1 and T_2 states are nearly degenerate ($\Delta E \approx 0.002$ eV), which promotes an efficient ISC from S_1 to T_2. This facilitates an efficient $S_1 \rightarrow T_2 \rightarrow T_1 \rightarrow S_0$ decay pathway, ultimately leading to phosphorescence.[136]

(3) Size effects: in a theoretical study of one-dimensional ultrathin rod-like ligand-protected gold nanoclusters (Au_{24}, Au_{42}, and Au_{60}), Luo and co-workers combined rate-constant calculations with multistate model analysis (Fig. 11B).[52] They showed that the size indirectly controls the emission type by modulating the SOC effect. The smaller Au_{24} cluster exhibits dual fluorescence, attributable to substantial excited-state structural distortion that creates two minima (S_1-MIN1 and S_1-MIN2) on the S_1 potential energy surface. These minima yield large ΔE_{ST} values (0.5 eV and 0.81 eV, respectively), which render ISC negligible. By contrast, for the longer rod-like clusters Au_{42} and Au_{60}, the large transition dipole moments lead to fluorescence radiative rates ($1.13 \times 10^8\ s^{-1}$ and $1.71 \times 10^8\ s^{-1}$, respectively) comparable to ISC rates ($1.23 \times 10^8\ s^{-1}$ and $8.68 \times 10^8\ s^{-1}$, respectively). Together with larger ΔE_{ST} values (0.39 eV and 0.57 eV) that suppress RISC, the result is dual emission comprising fluorescence and phosphorescence.

(4) Ligand substituent effects: rate-constant calculations were performed on chiral Au(I)Cu(I) clusters protected by NHC ligands (R/S-py-X and R/S-ql-X, X = Cl, Br, I) to investigate the effect of the halide substituent (Fig. 13).[133] The results show that as the halogen atomic mass increases, the $\Delta E_{ST}(S_1–T_1)$ narrows systematically (Fig. 13A): the R-ql-Cl cluster (0.294 eV), R-ql-Br cluster (0.193 eV), and R-ql-I cluster (0.116 eV). This narrowing of the $\Delta E_{ST}(S_1–T_1)$ corresponds to an increase in the RISC rate constant: R-ql-I ($7.05 \times 10^{10}\ s^{-1}$) > R-ql-Br ($4.22 \times 10^9\ s^{-1}$) > R-ql-Cl ($5.49 \times 10^8\ s^{-1}$). Consequently, the R-ql-I cluster exhibits the most efficient TADF owing to its minimal $\Delta E_{ST}(S_1–T_1)$.

In summary, recent studies establish that SOC, ISC, and RISC are pivotal in determining the photoluminescence of metal nanoclusters. The interaction between singlet and triplet

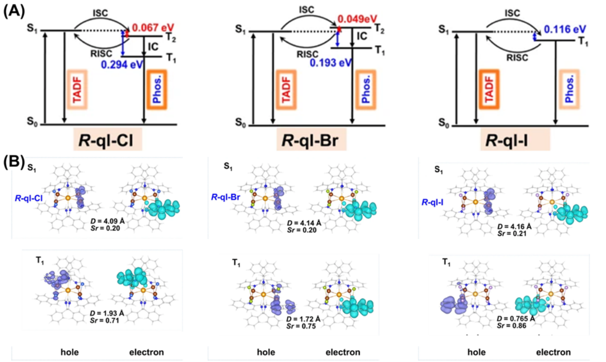

Fig. 13 (A) Energy diagram of R-ql-Cl, R-ql-Br, and R-ql-I indicating TADF and phosphorescence emission processes. (B) The hole and electron pairs for S_1/S_0 and T_1/S_0 transitions were obtained by NTO analysis at the optimized S_1 and T_1 geometries of R-ql-Cl, R-ql-Br, and R-ql-I (isovalue of 0.02). Au, yellow; Cu, brown; N, dark blue; C, gray; Cl, blue; Br, green; I, light purple; H, white. Reproduced with permission.[133] Copyright 2023, Springer Nature.

states, which is quantified by SOCMEs and the ΔE_{ST}, governs the competition among fluorescence, phosphorescence, and TADF, thereby shaping the quantum yield and lifetime. Structural factors, including cluster architecture, heteroatom doping, ligand identity and rigidity, and heavy-atom contributions, tune SOCMEs and ΔE_{ST} and also modulate nonradiative channels, producing outcomes ranging from single-channel emission to dual emission. These insights underscore the need for multi-state, rate-constant-based models that explicitly incorporate triplet states to explain and predict the diverse luminescent behaviors of metal nanoclusters.

4.3 Excited-state relaxation and nonradiative dynamics

Excited-state relaxation dynamics directly determine the cluster's excited-state lifetime and PLQY. These dynamics comprise IC and ISC among excited states, structural relaxation, charge transfer, and electron–hole recombination. Because such processes are not directly observable at the atomic scale, combining NA-MD with DFT/TDDFT enables atomistic elucidation of relaxation pathways, timescales, and nonradiative channels. Current research has successfully revealed how the ligand, metal core structure, and doping effects influence these excited-state relaxation dynamics.

By modifying the energy gap and orbital interactions, ligands regulate relaxation rates. TDDFT and NA-MD on $Au_{25}(SR)_{18}^-$ showed that internal relaxation among high-lying singlets ($S_6 \rightarrow S_1$) occurs on a sub-picosecond timescale, whereas the final $S_1 \rightarrow S_0$ decay is about two orders of magnitude slower.[126] Comparing $Au_{25}(SR)_{18}^-$ with different R groups (R = CH_3, C_2H_5, C_3H_7, MPA, PET) (MPA = mercaptopropionic acid) revealed S_1–S_6 relaxation times of 2–18 ps, with MPA producing distinctive dynamics due to a narrower LUMO+1–LUMO+2 gap.[137] For the phosphine-ligated $Au_{13}(dppe)_5Cl_2^{3+}$, which shares the Au_{13} core, NA-MD indicated a slower excited-state decay (0.5–20.3 ps) than in thiolate-protected $Au_{25}(SR)_{18}^-$, consistent with its larger HOMO–LUMO gap.[138] TDDFT and NA-MD on $Au_{38}(SR)_{24}$ further identified low-frequency vibrations, such as the 24.2 cm^{-1} bending mode, as key channels for electron–phonon coupling and nonradiative decay,[139] a behavior also observed in $Au_{18}(SH)_{14}$.[140] Notably, NA-MD simulations on $Au_{25}(SR)_{18}^-$ by Xie *et al.* revealed that low-frequency modes, particularly the breathing and stretching modes of Au(core)–Au(core) and Au(core)–Au(ring), are strongly coupled to the electronic transitions.[127] More recent NA-MD work shows that ligands can also modulate carrier lifetimes by altering SOC.[129] For example, thiolate-protected $Au_{25}(SR)_{18}^-$ relaxed in 99 fs, compared with 132 fs for the diphosphine-protected Au_{13}^{3+} cluster.[138]

Studies of $Au_{30}(SR)_{18}$, $Au_{36}(SR)_{24}$, $Au_{38}S_2(SR)_{20}$, and $Au_{44}(SR)_{28}$ demonstrate that core stacking adjusts excited-state relaxation.[141] $Au_{30}(SR)_{18}$ with a HCP core exhibits stronger electron–phonon coupling than $Au_{38}S_2(SR)_{20}$ with a body-centered cubic (BCC) core, resulting in a shorter lifetime. Additionally, nonadiabatic relaxation also depends on dopants.[142] Yu *et al.* combined DFT with time-domain NA-MD to examine single-atom doping in $MAu_{24}(SR)_{18}$ (M = Pd, Pt, Cd, Hg), showing that dopants co-regulate relaxation through changes in the gap, phonon spectrum, and electron–phonon coupling strength.[143] In diphosphine-ligated M@Au_{12} clusters, Ir doping enhances core–shell coupling and suppresses recombination, thereby extending the lifetime and confirming the dynamical impact of doping.[144]

Overall, real-time NA-MD based on DFT and TDDFT has become indispensable for resolving the excited-state dynamics of ligand-protected gold nanoclusters. These simulations show that larger electronic gaps lengthen lifetimes, stronger electron–phonon coupling accelerates nonradiative decay, and low-frequency vibrations critically mediate energy dissipation. Moreover, subtle structural variations, including isomerism[145] and single-atom doping, can markedly reshape relaxation behavior and photophysical properties.

5. Conclusions and outlook

In this review, we summarize recent experimental advances in enhancing the PLQY of ligand-protected gold nanoclusters, with emphasis on strategies that promote radiative decay and suppress nonradiative pathways. Experimentally, increasing the radiative rate constant *via* HOMO–LUMO gap engineering, achieved through heterometal doping to widen the HOMO–LUMO gap and through enhancement of transition dipole moments, has proven highly effective. Suppressing nonradiative relaxation by rigidifying and constraining ligand motion in core–shell structures has likewise yielded substantial gains in quantum efficiency. Nevertheless, a deeper mechanistic understanding of how transition dipole moments are enhanced is still needed to further improve radiative efficiency. In addition, most ligand-protected gold nanoclusters are soluble only in organic solvents, limiting biomedical applications; consequently, simple and general strategies to convert organo-soluble clusters into water-soluble forms are highly desirable.[64]

Theoretically, DFT/TDDFT methods and NA-MD have clarified photoluminescence origins, complex excited-state dynamics, and emission pathways—fluorescence, phosphorescence, TADF, and dual emission—governed by ΔE_{ST}, SOCMEs, and structural relaxation. Even so, improving the computational efficiency of excited-state optimizations and vibrational analyses remains essential, particularly for large clusters.[146,147] Computing radiative and nonradiative rate constants has deepened the understanding of competing decay channels, yet accurately predicting PLQYs is still challenging. Looking ahead, multiscale modeling that incorporates environmental effects such as solvent and matrix interactions will provide more realistic descriptions.[66–70] Moreover, machine-learning approaches trained on high-level quantum-chemical data promise to accelerate the discovery and screening of ligands, dopants, and structural motifs with desirable photophysical properties.[148–154]

Author contributions

All authors contributed to writing and editing this article.

Conflicts of interest

There are no conflicts to declare.

Data availability

No primary research results, software or code have been included and no new data were generated or analysed as part of this review.

Acknowledgements

The authors acknowledge financial support from NSFC (22373082), the science and technology innovation program of Hunan Province (2023RC1055), the project of innovation team of the ministry of education (IRT_17R90), and the Scientific Research Fund of Hunan Provincial Education Department (22B0154).

References

1 K. Zheng and J. Xie, *Acc. Mater. Res.*, 2021, **2**, 1104–1116.
2 Z. Guo, G. Yu, Z. Zhang, Y. Han, G. Guan, W. Yang and M. Y. Han, *Adv. Mater.*, 2023, e2206700.
3 Y. Huang, K. Chen, L. Liu, H. Ma, X. Zhang, K. Tan, Y. Li, Y. Liu, C. Liu, H. Wang and X.-D. Zhang, *Small*, 2023, **19**, 2300145.
4 A. Baghdasaryan and H. Dai, *Chem. Rev.*, 2025, **125**, 5195–5227.
5 J. Yang, F. Yang, C. Zhang, X. He and R. Jin, *ACS Mater. Lett.*, 2022, **4**, 1279–1296.
6 Z. Yang, X. Yang, Y. Guo and H. Kawasaki, *ACS Appl. Bio Mater.*, 2023, **6**, 4504–4517.
7 N. Sharma, W. Mohammad, X. Le Guével and A. Shanavas, *Chem. Biomed. Imaging*, 2024, **2**, 462–480.
8 S. Takano, H. Hirai, T. Nakashima, T. Iwasa, T. Taketsugu and T. Tsukuda, *J. Am. Chem. Soc.*, 2021, **143**, 10560–10564.
9 K. Mutoh, T. Yahagi, S. Takano, S. Kawakita, T. Iwasa, T. Taketsugu, T. Tsukuda and T. Nakashima, *Chem. Sci.*, 2025, **16**, 8240–8246.
10 V. K. Kulkarni, E. L. Albright, E. Zeinizade, E. Steele, J. Chen, L. Ding, S. Malola, S. Takano, K. Harrington, N. Kwon, T. I. Levchenko, M. Nambo, T. Tsukuda, H. Häkkinen, K. Stamplecoskie, G. Zheng and C. M. Crudden, *J. Am. Chem. Soc.*, 2025, **147**, 4017–4025.
11 W.-Q. Shi, L. Zeng, R.-L. He, X.-S. Han, Z.-J. Guan, M. Zhou and Q.-M. Wang, *Science*, 2024, **383**, 326–330.
12 L. Luo, Z. Liu, A. Mazumder and R. Jin, *J. Am. Chem. Soc.*, 2024, **146**, 27993–27997.
13 X. Wang, Y. Zhong, T. Li, K. Wang, W. Dong, M. Lu, Y. Zhang, Z. Wu, A. Tang and X. Bai, *Nat. Commun.*, 2025, **16**, 587.
14 J. S. Yang, Y. J. Zhao, X. M. Li, X. Y. Dong, Y. B. Si, L. Y. Xiao, J. H. Hu, Z. Yu and S. Q. Zang, *Angew Chem. Int. Ed. Engl.*, 2024, **63**, e202318030.
15 K. Yoshida, D. Arima and M. Mitsui, *J. Phys. Chem. Lett.*, 2023, **14**, 10967–10973.
16 W. Zhang, L. Luo, Z. Liu, F. Zhao, J. Kong, R. Jin, Y. Luo and M. Zhou, *Sci. Adv.*, 2025, **11**, eadx2781.
17 Z. Liu, L. Luo, J. Kong, E. Kahng, M. Zhou and R. Jin, *Nanoscale*, 2024, **16**, 7419–7426.
18 Z. Liu, L. Luo and R. Jin, *Adv. Mater.*, 2024, **36**, e2309073.
19 L. Luo, Z. Liu, X. Du and R. Jin, *Commun. Chem.*, 2023, **6**, 22.
20 A. Mazumder, K. Li, Z. Liu, Y. Wang, Y. Pei, L. A. Peteanu and R. Jin, *ACS Nano*, 2024, **18**, 21534–21543.
21 C. Zhu, Z.-L. Chen, H. Li, L. Lu, X. Kang, J. Xuan and M. Zhu, *J. Am. Chem. Soc.*, 2024, **146**, 23212–23220.
22 W.-D. Si, C. Zhang, M. Zhou, W.-D. Tian, Z. Wang, Q. Hu, K.-P. Song, L. Feng, X.-Q. Huang, Z.-Y. Gao, C.-H. Tung and D. Sun, *Sci. Adv.*, 2023, **9**, eadg3587.
23 W. D. Si, C. Zhang, M. Zhou, Z. Wang, L. Feng, C. H. Tung and D. Sun, *Sci. Adv.*, 2024, **10**, eadm6928.
24 H. Lin, X. Song, O. J. H. Chai, Q. Yao, H. Yang and J. Xie, *Adv. Mater.*, 2024, e2401002.
25 Q. Li, C. J. t. Zeman, B. Kalkan, K. Kirschbaum, C. G. Gianopoulos, A. Parakh, D. Doan, A. C. Lee, J. Kulikowski, G. C. Schatz, G. Shen, M. Kunz and X. W. Gu, *Nano Lett.*, 2023, **23**, 132–139.
26 L. Zhang, D. Fan, Y. Shi, S. He, M. Cui, H. Yu and M. Zhu, *RSC Adv.*, 2023, **13**, 16034–16038.
27 Y. Zhou, L. Liao, S. Zhuang, Y. Zhao, Z. Gan, W. Gu, J. Li, H. Deng, N. Xia and Z. Wu, *Angew. Chem., Int. Ed.*, 2021, **60**, 8668–8672.
28 Y. Wang, C. G. Gianopoulos, Z. Liu, K. Kirschbaum, D. Alfonso, D. R. Kauffman and R. Jin, *JACS Au*, 2024, **4**, 1928–1934.
29 M. Suyama, S. Takano and T. Tsukuda, *J. Phys. Chem. C*, 2020, **124**, 23923–23929.
30 H. Hirai, S. Takano, T. Nakashima, T. Iwasa, T. Taketsugu and T. Tsukuda, *Angew Chem. Int. Ed. Engl.*, 2022, **61**, e202207290.
31 Z. Liu, M. Zhou, L. Luo, Y. Wang, E. Kahng and R. Jin, *J. Am. Chem. Soc.*, 2023, **145**, 19969–19981.

32 B. Zhang, J. Chen, Y. Cao, O. J. H. Chai and J. Xie, *Small*, 2021, **17**, e2004381.
33 A. Kim, C. Zeng, M. Zhou and R. Jin, *Part. Part. Syst. Charact.*, 2017, **34**, 1600388.
34 Y. Wang, Z. Liu, A. Mazumder, C. G. Gianopoulos, K. Kirschbaum, L. A. Peteanu and R. Jin, *J. Am. Chem. Soc.*, 2023, **145**, 26328–26338.
35 S. Kim, H. Kim, C. Lee, I. Park, Y. Kim, D. Moon, J. H. Shim, S. Ryu and S. S. Park, *ACS Nano*, 2024, **18**, 29036–29044.
36 H. Chang, N. S. Karan, K. Shin, M. S. Bootharaju, S. Nah, S. I. Chae, W. Baek, S. Lee, J. Kim, Y. J. Son, T. Kang, G. Ko, S.-H. Kwon and T. Hyeon, *J. Am. Chem. Soc.*, 2020, **143**, 326–334.
37 Z. Luo, X. Yuan, Y. Yu, Q. Zhang, D. T. Leong, J. Y. Lee and J. Xie, *J. Am. Chem. Soc.*, 2012, **134**, 16662–16670.
38 D. A. Buschmann, H. Hirai and T. Tsukuda, *Inorg. Chem. Front.*, 2024, **11**, 6694–6710.
39 X. Du, T. Higaki, H. Ma, X. Zhang, G. Wang, H. Wang and R. Jin, *Nanoscale*, 2025, **17**, 14408–14414.
40 L. Luo, Z. Liu, J. Kong, C. G. Gianopoulos, I. Coburn, K. Kirschbaum, M. Zhou and R. Jin, *Proc. Natl. Acad. Sci. U. S. A.*, 2024, **121**, e2318537121.
41 M. Zhou, T. Higaki, Y. Li, C. Zeng, Q. Li, M. Y. Sfeir and R. Jin, *J. Am. Chem. Soc.*, 2019, **141**, 19754–19764.
42 J. Wei, J. F. Halet, S. Kahlal, J. Y. Saillard and A. Munoz-Castro, *Inorg. Chem.*, 2020, **59**, 15240–15249.
43 A. Fihey, F. Maurel and A. Perrier, *J. Phys. Chem. C*, 2014, **118**, 4444–4453.
44 T. Song, J. Kong, S. Tang, X. Cai, X. Liu, M. Zhou, W. W. Xu, W. Ding and Y. Zhu, *Nano Res.*, 2023, **16**, 19754–19764.
45 H. Hirai, S. Takano, T. Nakamura and T. Tsukuda, *Inorg. Chem.*, 2020, **59**, 17889–17895.
46 S. Wang, X. Meng, A. Das, T. Li, Y. Song, T. Cao, X. Zhu, M. Zhu and R. Jin, *Angew. Chem., Int. Ed.*, 2014, **53**, 2376–2380.
47 S. Takano and T. Tsukuda, *J. Am. Chem. Soc.*, 2021, **143**, 1683–1698.
48 Q. Li, C. J. Zeman, G. C. Schatz and X. W. Gu, *ACS Nano*, 2021, **15**, 16095–16105.
49 K. Li, P. Wang and Y. Pei, *J. Phys. Chem. Lett.*, 2024, **15**, 9216–9225.
50 L. Luo, Z. Liu, X. Du and R. Jin, *J. Am. Chem. Soc.*, 2022, **144**, 19243–19247.
51 X. Y. Xie, K. Q. Cheng, W. K. Chen, W. Li, Q. Li, J. Han, W. H. Fang and G. Cui, *J. Phys. Chem. Lett.*, 2023, **14**, 10025–10031.
52 Y. Luo, K. Li, P. Wang and Y. Pei, *JACS Au*, 2025, **5**, 4593–4603.
53 Z. Ma, P. Wang, G. Zhou, J. Tang, H. Li and Y. Pei, *J. Phys. Chem. C*, 2016, **120**, 13739–13748.
54 B. Li, L. Kang, Y. Lun, J. Yu, S. Song and Y. Wang, *Carbon Energy*, 2024, **6**, e547.
55 Y. Pei, P. Wang, Z. Ma and L. Xiong, *Acc. Chem. Res.*, 2019, **52**, 23–33.
56 S. Hossain, D. Hirayama, A. Ikeda, M. Ishimi, S. Funaki, A. Samanta, T. Kawawaki and Y. Negishi, *Aggregate*, 2022, **4**, e255.
57 Y. Negishi, S. Hashimoto, A. Ebina, K. Hamada, S. Hossain and T. Kawawaki, *Nanoscale*, 2020, **12**, 8017–8039.
58 R. H. Adnan, J. M. L. Madridejos, A. S. Alotabi, G. F. Metha and G. G. Andersson, *Adv. Sci.*, 2022, **9**, e2105692.
59 Z. Lei, X.-K. Wan, S.-F. Yuan, Z.-J. Guan and Q.-M. Wang, *Acc. Chem. Res.*, 2018, **51**, 2465–2474.
60 E. L. Albright, T. I. Levchenko, V. K. Kulkarni, A. I. Sullivan, J. F. DeJesus, S. Malola, S. Takano, M. Nambo, K. Stamplecoskie, H. Hakkinen, T. Tsukuda and C. M. Crudden, *J. Am. Chem. Soc.*, 2024, **146**, 5759–5780.
61 M. R. Narouz, K. M. Osten, P. J. Unsworth, R. W. Y. Man, K. Salorinne, S. Takano, R. Tomihara, S. Kaappa, S. Malola, C. T. Dinh, J. D. Padmos, K. Ayoo, P. J. Garrett, M. Nambo, J. H. Horton, E. H. Sargent, H. Hakkinen, T. Tsukuda and C. M. Crudden, *Nat. Chem.*, 2019, **11**, 419–425.
62 P. Luo, X. J. Zhai, S. Bai, Y. B. Si, X. Y. Dong, Y. F. Han and S. Q. Zang, *Angew. Chem., Int. Ed.*, 2023, **62**, e202219017.
63 N. N. Eyyakkandy, A. Afreen, G. Vilangappurath, S. Gratious, K. V. Adarsh and S. Mandal, *J. Phys. Chem. C*, 2024, **128**, 18828–18835.
64 A. I. Sullivan, E. A. Steele, S. Takano, E. Zeinizade, J. Chen, S. Malola, K. Siddhant, H. Häkkinen, K. G. Stamplecoskie, T. Tsukuda, G. Zheng and C. M. Crudden, *J. Am. Chem. Soc.*, 2025, **147**, 4230–4238.
65 Z. Liu, Y. Wang, W. Ji, X. Ma, C. G. Gianopoulos, S. Calderon, T. Ma, L. Luo, A. Mazumder, K. Kirschbaum, E. C. Dickey, L. A. Peteanu, D. Alfonso and R. Jin, *ACS Nano*, 2025, **19**, 9121–9131.
66 T. Eskelinen and A. J. Karttunen, *Inorg. Chem.*, 2025, **64**, 9150–9162.
67 Y.-J. Gao, W.-K. Chen, Z.-R. Wang, W.-H. Fang and G. Cui, *Phys. Chem. Chem. Phys.*, 2018, **20**, 24955–24967.
68 Q. Wang, Y.-J. Gao, T.-T. Zhang, J. Han and G. Cui, *RSC Adv.*, 2019, **9**, 20786–20795.
69 J. Liu and X. He, *Wiley Interdiscip. Rev.: Comput. Mol. Sci.*, 2023, **13**, e1650.
70 H. Li, T. Wang, J. Han, Y. Xu, X. Kang, X. Li and M. Zhu, *Nat. Commun.*, 2024, **15**, 5351.
71 G. Cui and W. Thiel, *J. Chem. Phys.*, 2014, **141**, 124101.
72 Y.-G. Fang, L.-Y. Peng, X.-Y. Liu, W.-H. Fang and G. Cui, *Comput. Theor. Chem.*, 2019, **1155**, 90–100.
73 K. Pyo, V. D. Thanthirige, K. Kwak, P. Pandurangan, G. Ramakrishna and D. Lee, *J. Am. Chem. Soc.*, 2015, **137**, 8244–8250.
74 Y. Chen, M. Zhou, Q. Li, H. Gronlund and R. Jin, *Chem. Sci.*, 2020, **11**, 8176–8183.
75 N. Xia, J. Yuan, L. Liao, W. Zhang, J. Li, H. Deng, J. Yang and Z. Wu, *J. Am. Chem. Soc.*, 2020, **142**, 12140–12145.
76 J. Dong, Z. Gan, W. Gu, Q. You, Y. Zhao, J. Zha, J. Li, H. Deng, N. Yan and Z. Wu, *Angew Chem. Int. Ed. Engl.*, 2021, **60**, 17932–17936.
77 H. Deng, K. Huang, L. Xiu, W. Sun, Q. Yao, X. Fang, X. Huang, H. A. A. Noreldeen, H. Peng, J. Xie and W. Chen, *Nat. Commun.*, 2022, **13**, 3381.
78 Z. Liu, T. Lu and Q. Chen, *Carbon*, 2020, **165**, 461–467.

79 J. She, W. Pei, S. Zhou and J. Zhao, *J. Phys. Chem. Lett.*, 2022, **13**, 5873–5880.

80 P. N. Day, R. Pachter, K. A. Nguyen and R. Jin, *J. Phys. Chem. A*, 2019, **123**, 6472–6481.

81 F. Muniz-Miranda, M. C. Menziani and A. Pedone, *J. Phys. Chem. A*, 2015, **119**, 5088–5098.

82 H. Baek, J. Moon and J. Kim, *J. Phys. Chem. A*, 2017, **121**, 2410–2419.

83 F. Muniz-Miranda, M. C. Menziani and A. Pedone, *J. Phys. Chem. C*, 2014, **118**, 7532–7544.

84 J. P. Perdew, *Phys. Rev. B:Condens. Matter Mater. Phys.*, 1986, **33**, 8822–8824.

85 J. P. Perdew, K. Burke and M. Ernzerhof, *Phys. Rev. Lett.*, 1996, **77**, 3865–3868.

86 J. Tao, J. P. Perdew, V. N. Staroverov and G. E. Scuseria, *Phys. Rev. Lett.*, 2003, **91**, 146401.

87 J. P. Perdew, J. Tao, V. N. Staroverov and G. E. Scuseria, *J. Chem. Phys.*, 2004, **120**, 6898–6911.

88 C. Adamo and V. Barone, *J. Chem. Phys.*, 1999, **110**, 6158–6170.

89 A. D. Becke, *J. Chem. Phys.*, 1992, **96**, 2155–2160.

90 P. J. Stephens, F. J. Devlin, C. F. Chabalowski and M. J. Frisch, *J. Phys. Chem.*, 1994, **98**, 11623–11627.

91 Y. Zhang and W. Yang, *Phys. Rev. Lett.*, 1998, **80**, 890.

92 V. N. Staroverov, G. E. Scuseria, J. Tao and J. P. Perdew, *J. Chem. Phys.*, 2003, **119**, 12129–12137.

93 S. Grimme, *J. Phys. Chem. A*, 2005, **109**, 3067–3077.

94 Y. Zhao and D. G. Truhlar, *Theor. Chem. Acc.*, 2008, **120**, 215–241.

95 T. Yanai, D. P. Tew and N. C. Handy, *Chem. Phys. Lett.*, 2004, **393**, 51–57.

96 D. Jacquemin, E. A. Perpète, I. Ciofini and C. Adamo, *Theor. Chem. Acc.*, 2011, **128**, 127–136.

97 Y. Luo, P. Wang and Y. Pei, *J. Phys. Chem. Lett.*, 2025, **16**, 3705–3714.

98 L. Qian, Y. Gao, C. Xu and L. Cheng, *J. Phys. Chem. Lett.*, 2025, **16**, 8683–8689.

99 A. V. Krukau, O. A. Vydrov, A. F. Izmaylov and G. E. Scuseria, *J. Chem. Phys.*, 2006, **125**, 224106.

100 K. L. D. M. Weerawardene and C. M. Aikens, *J. Am. Chem. Soc.*, 2016, **138**, 11202–11210.

101 S. Havenridge and C. M. Aikens, *J. Chem. Phys.*, 2021, **155**, 074302.

102 R. Rüger, E. van Lenthe, T. Heine and L. Visscher, *J. Chem. Phys.*, 2016, **144**, 184103.

103 Y. Wang, S. Havenridge and C. M. Aikens, *J. Chem. Phys.*, 2024, **161**, 024101.

104 L. Wu, W. Fang and X. Chen, *Phys. Chem. Chem. Phys.*, 2016, **18**, 17320–17325.

105 V. Veryazov, P. Å. Malmqvist and B. O. Roos, *Int. J. Quantum Chem.*, 2011, **111**, 3329–3338.

106 K. Veys, M. H. E. Bousquet, D. Jacquemin and D. Escudero, *J. Chem. Theory Comput.*, 2023, **19**, 9344–9357.

107 Z. Shuai, *Chin. J. Chem.*, 2020, **38**, 1223–1232.

108 A. Humeniuk, M. Buzancic, J. Hoche, J. Cerezo, R. Mitric, F. Santoro and V. Bonacic-Koutecky, *J. Chem. Phys.*, 2020, **152**, 054107.

109 R. Englman and J. Jortner, *Mol. Phys.*, 1970, **18**, 145–164.

110 M. Hagai, N. Inai, T. Yasuda, K. J. Fujimoto and T. Yanai, *Sci. Adv.*, 2024, **10**, eadk3219.

111 T. J. Penfold, E. Gindensperger, C. Daniel and C. M. Marian, *Chem. Rev.*, 2018, **118**, 6975–7025.

112 Q. Peng, Y. Niu, Q. Shi, X. Gao and Z. Shuai, *J. Chem. Theory Comput.*, 2013, **9**, 1132–1143.

113 C. M. Marian, *Wiley Interdiscip. Rev.: Comput. Mol. Sci.*, 2011, **2**, 187–203.

114 M. Etinski, J. Tatchen and C. M. Marian, *J. Chem. Phys.*, 2011, **134**, 154105.

115 J. Cerezo and F. Santoro, *J. Comput. Chem.*, 2023, **44**, 626–643.

116 R. R. Valiev, B. S. Merzlikin, R. T. Nasibullin, A. Kurtzevitch, V. N. Cherepanov, R. R. Ramazanov, D. Sundholm and T. Kurten, *Phys. Chem. Chem. Phys.*, 2023, **25**, 6406–6415.

117 S. H. Lin, W. Z. Xiao and W. Dietz, *Phys. Rev. E*, 1993, **47**, 3698–3706.

118 S. H. Lin, *J. Chem. Phys.*, 1966, **44**, 3759–3767.

119 C. R. Mulvihill, Y. Georgievskii and S. J. Klippenstein, *J. Chem. Phys.*, 2023, **159**, 174104.

120 Y. Wang, J. Ren and Z. Shuai, *J. Chem. Phys.*, 2021, **154**, 214109.

121 M. B. Ousmanou, J. Z. Yohana, F. Tchangnwa Nya, A. Malloum and J. Conradie, *Mater. Sci. Semicond. Process.*, 2025, **185**, 108894.

122 R. A. Marcus, *Rev. Mod. Phys.*, 1993, **65**, 599–610.

123 D. Beljonne, Z. Shuai, G. Pourtois and J. L. Bredas, *J. Phys. Chem. A*, 2001, **105**, 3899–3907.

124 A. Köhler and H. Bässler, *Mater. Sci. Eng., R*, 2009, **66**, 71–109.

125 X. Chen, O. V. Prezhdo, Z. Ma, T. Hou, Z. Guo and Y. Li, *Phys. Status Solidi B*, 2016, **253**, 458–462.

126 R. D. Senanayake, A. V. Akimov and C. M. Aikens, *J. Phys. Chem. C*, 2017, **121**, 10653–10662.

127 J. Xie, W. Li and Y. Pei, *J. Phys. Chem. Lett.*, 2025, **16**, 11259–11266.

128 X. Y. Liu, W. K. Chen, W. H. Fang and G. Cui, *J. Chem. Theory Comput.*, 2023, **19**, 8491–8522.

129 Y. Zhou, J. Zhou, X. Yu, W. Pei, S. Zhou and J. Zhao, *J. Phys. Chem. Lett.*, 2025, **16**, 8613–8620.

130 S. A. Miller, J. M. Womick, J. F. Parker, R. W. Murray and A. M. Moran, *J. Phys. Chem. C*, 2009, **113**, 9440–9444.

131 K. L. D. M. Weerawardene, E. B. Guidez and C. M. Aikens, *J. Phys. Chem. C*, 2017, **121**, 15416–15423.

132 S. Havenridge and C. M. Aikens, *J. Phys. Chem. A*, 2023, **127**, 9932–9943.

133 X.-H. Ma, J. Li, P. Luo, J.-H. Hu, Z. Han, X.-Y. Dong, G. Xie and S.-Q. Zang, *Nat. Commun.*, 2023, **14**, 4121.

134 W.-M. He, J.-H. Hu, Y.-J. Cui, J. Li, Y.-B. Si, S.-B. Wang, Y.-J. Zhao, Z. Zhou, L.-F. Ma and S.-Q. Zang, *Natl. Sci. Rev.*, 2024, **11**, nwae174.

135 J. Li, P. Wang and Y. Pei, *J. Phys. Chem. Lett.*, 2022, **13**, 3718–3725.

136 C. Zhu, J. Xin, J. Li, H. Li, X. Kang, Y. Pei and M. Zhu, *Angew. Chem.*, 2022, **134**, e202205947.

137 R. D. Senanayake and C. M. Aikens, *Phys. Chem. Chem. Phys.*, 2020, **22**, 5272–5285.

138 K. L. D. M. Weerawardene, P. Pandeya, M. Zhou, Y. Chen, R. Jin and C. M. Aikens, *J. Am. Chem. Soc.*, 2019, **141**, 18715–18726.

139 R. D. Senanayake, E. B. Guidez, A. J. Neukirch, O. V. Prezhdo and C. M. Aikens, *J. Phys. Chem. C*, 2018, **122**, 16380–16388.

140 R. D. Senanayake and C. M. Aikens, *J. Chem. Phys.*, 2019, **151**, 094702.

141 X. Yu, W. Pei, W. W. Xu, Y. Zhao, Y. Su and J. Zhao, *Inorg. Chem.*, 2023, **62**, 20450–20457.

142 P. Pandeya, R. D. Senanayake and C. M. Aikens, *J. Chem. Phys.*, 2021, **154**, 184303.

143 X. Yu, Y. Sun, W.-w. Xu, J. Fan, J. Gao, X. Jiang, Y. Su and J. Zhao, *Nanoscale Horiz.*, 2022, **7**, 1192–1200.

144 W. Pei, L. Hou, J. Yang, S. Zhou and J. Zhao, *Nanoscale*, 2024, **16**, 14081–14088.

145 Y. Sun, X. Yu, P. Liu, W. Han, W.-w. Xu, Y. Su and J. Zhao, *Nanotechnology*, 2022, **34**, 105701.

146 W. K. Chen, W. H. Fang and G. Cui, *J. Chem. Phys.*, 2023, **158**, 044110.

147 J. Du, K. Liao, J. Ma, W. Li and S. Li, *J. Chem. Theory Comput.*, 2022, **18**, 7630–7638.

148 C. A. McCandler, A. Pihlajamäki, S. Malola, H. Häkkinen and K. A. Persson, *ACS Nano*, 2024, **18**, 19014–19023.

149 A. Karmakar, Dhananjay and T. Karmakar, *Nano Lett.*, 2025, **25**, 10187–10192.

150 T. Chen, J. Li, P. Cai, Q. Yao, Z. Ren, Y. Zhu, S. Khan, J. Xie and X. Wang, *Nano Res.*, 2022, **16**, 4188–4196.

151 L. Fang, J. Laakso, P. Rinke and X. Chen, *J. Chem. Phys.*, 2024, **160**, 094106.

152 A. Pihlajamäki, J. Hämäläinen, J. Linja, P. Nieminen, S. Malola, T. Kärkkäinen and H. Häkkinen, *J. Phys. Chem. A*, 2020, **124**, 4827–4836.

153 V. Tiwari and T. Karmakar, *Nano Lett.*, 2025, **25**, 5940–5946.

154 Y. Wang, D. S. N. D. Samarasinghe, H. Deng, B. Liu and C. M. Aikens, *J. Chem. Inf. Model.*, 2025, **65**, 3892–3902.